

A NURBS-based Parametric Method Bridging Mesh-free and Finite Element Formulations

Amit Shaw¹, B. Banerjee¹ and D Roy^{1,2}

Abstract: A generalization of a NURBS based parametric mesh-free method (NPMM), recently proposed by Shaw and Roy (2008), is considered. A key feature of this parametric formulation is a geometric map that provides a local bijection between the physical domain and a rectangular parametric domain. This enables constructions of shape functions and their derivatives over the parametric domain whilst satisfying polynomial reproduction and interpolation properties over the (non-rectangular) physical domain. Hence the NPMM enables higher-dimensional B-spline based functional approximations over non-rectangular domains even as the NURBS basis functions are constructed via the usual tensor products of their one-dimensional counterparts. Nevertheless the method still lacks the universality that the FEM enjoys. In particular, for many non-simply connected domains, the geometric map may not be locally bijective everywhere and this severely restricts the general applicability of the NPMM. In this paper, a piecewise form of the NPMM is proposed, wherein the domain is decomposed into a collection of simply connected sub-domains or element patches (analogous to the FEM). The NPMM is then employed over each sub-domain without affecting the continuity of approximated functions across inter-sub-domain boundaries. This is quite unlike the usual FEM. The proposed procedure not only possesses the generality of the FEM, it is also equipped with higher order, globally smooth and interpolating basis functions. It may thus be interpreted as a seamless bridge between the FEM and mesh-free methods. In the context of weak implementations of the piecewise NPMM, we propose a confor-

mal knot-grid integration scheme. Finally, we illustrate these schemes for weak numerical solutions of a few linear and nonlinear boundary value problems of engineering interest.

Keyword: NURBS; parametric mesh-free methods; reproducing kernels; finite element analysis; geometric map; solid mechanics.

1 The Introduction

In any engineering analysis the accuracy and the cost of computation may get affected by the procedure employed for domain and functional discretizations. In the context of the FEM, these requirements are generally not adequately attended to because of a crude approximation of the original geometry, an expensive mesh generation especially for a complicated geometry, and a poor element-wise approximation of the field variable(s) with a loss of inter-element continuity. A way out of some of these drawbacks is however possible with mesh-free methods - a more recent development. These methods, unlike classical forms of the FEM, do not require an element-based mesh generation for the discretization of domain geometries. The entire domain is discretized by a set of grid points (also called nodes or particles). Constructions of mesh-free shape functions have been well researched over the last two decades. Mention may, in particular, be made of the smooth particle hydrodynamics (SPH), (Lucy 1977; Gingold and Monaghan 1977, Monaghan 1992), diffuse element method (DEM) (Nayrole *et al.* 1992), element free Galerkin method (EFG) (Belytschko *et al.* 1994, Lu *et al.* 1994), reproducing kernel particle method (RKPM) (Liu *et al.* 1995a, 1995b), moving least square reproducing kernel

¹ Structures Lab, Department of Civil Engineering, Indian Institute of Science, Bangalore 560012, India

² Corresponding author. Email: royd@civil.iisc.ernet.in

(MLSRK) method (Liu *et al.* 1997), partition of unity method (PUM) (Babuška and Melenk 1997, Melenk and Babuška 1996), $h - p$ clouds (Duarte and Oden 1997), mesh-free local boundary integral equation method (LBIE) (Zhu *et al.* 1998), mesh-free local Petrov–Galerkin method (MLPG) (Atluri and Zhu 1998, Atluri and Shen 2002, Atluri *et al.* 1999, 2004, 2006a, b), point interpolation method (Liu and Gu 2001a, b, c), boundary point interpolation methods (Gu and Liu 2001), radial point interpolation method (Dai *et al.* 2004), reproducing kernel element method (Liu *et al.* 2004, Li *et al.* 2004, Lu *et al.* 2004, Simkins *et al.* 2004), reproducing kernel interpolating method (2007b), error reproducing kernel method (ERKM) (Shaw and Roy 2007a), error reproducing and interpolating kernel method (ERIKM) (Shaw *et al.* 2008) and several others. For a comprehensive review of mesh-free methods, readers are suggested to refer (Li and Liu 2002, Fries and Matthies 2004).

However, despite the ability to dispense with the discretization through elements, the evaluation of mesh-free shape functions and their use in constructing the trial and test spaces (as in a Galerkin formulation) may lead to some other computational as well as numerical difficulties. First, since most mesh-free shape functions do not satisfy the Kronecker delta property and fail to vanish at the essential boundaries, the imposition of essential boundary conditions is not as trivial (Fernández-Méndez and Huerta 2004), unlike the FEM. Second, there may be a misalignment of the support of a shape function with the integration cell (required for evaluating the integrals in the weak form) which makes the method non-conforming. Third, most mesh-free schemes are based on a discrete and approximated form of the integral kernel representation of a function. Generally the user needs to optimize the size of the kernel (window) function based on some numerical experiments. A mesh-free approximation with automatically and uniquely obtainable support size (for a given nodal distribution) has so far been elusive.

In an effort to address some of these difficulties, Shaw and Roy (2007a) have recently proposed a NURBS (non-uniform rational B-spline) based

error reproducing kernel method (ERKM). In ERKM, the target function is first approximated via NURBS basis functions. Then the error (remainder) function, resulting from the NURBS approximation of the target function, is reproduced (within a finite-dimensional polynomial space) through a non-NURBS family of basis functions and added to the NURBS approximation of the target function. Error reproducing and interpolating kernel method (ERIKM), an interpolating version of ERKM based on Kriging, has also been developed (Shaw *et al.* 2008). The ERKM and ERIKM have several attractive features owing to the usage of NURBS, such as near-insensitivity to support sizes of the window functions and the ability to represent sharp changes (such as shocks) without numerical instability. Unfortunately since NURBS in higher dimension (> 1) is constructed via the tensor product of one dimensional functions, it is only defined over a d -dimensional hypercube (square in \mathbb{R}^2 and a cuboid in \mathbb{R}^3). Hence, in most problems of practical interest, the geometric complexity of the domain prevents making use of NURBS in the ERKM/ERIKM. In order to realize the objective of dealing with a domain with irregular geometry, a NURBS-based parametric mesh-free method (NPMM) has been proposed (Shaw and Roy 2008). Here, NURBS basis functions are constructed over a parametric space $\bar{\Omega} = [0, 1]^n$ (n is the dimension of the domain) such that reproduction and interpolation properties are satisfied over the (non-rectangular) physical domain $\Omega_c = \Omega \cup \partial\Omega$ and the geometric map $F : \bar{\Omega} \rightarrow \Omega_c$ is simultaneously preserved. Needless to say, the geometric map F plays a crucial role in the parametric formulation. However, for many (probably most) physical domains of practical interest, a bijective may not exist. This severely restricts the applicability of the NPMM.

As a way out of these difficulties and towards further generalization of the method, we presently explore a spatially piecewise form of the NPMM. The first key step is to decompose the physical domain $\Omega_c = \Omega \cup \partial\Omega \subset \mathbb{R}^n$ into a finite number of sub-domains or element patches $\{\Omega_c^e\}_{e=1}^{N^e}$ such that there is a family of local bijections $F^e : \bar{\Omega}^e \rightarrow \Omega_c^e \forall e \in [1, N^e]$. Here $\bar{\Omega} = [0, 1]^d \subset \mathbb{R}^d$ ($d \leq n$) is

the so-called parametric domain, a d -dimensional hypercube. Then each parametric domain $\overline{\Omega}^e$ is discretized (into NURBS cells), which is transferred to the element patch Ω_c^e via F^e . Once the physical domain is discretized, a set of NURBS-based basis functions are constructed over $\overline{\Omega}^e$ so that polynomial reproduction properties are satisfied over each Ω_c^e without affecting the continuity of approximated functions across the boundaries of the element patches. However, like any other numerical scheme, improper implementations of the piecewise NPMM may affect the accuracy and convergence of the solution. In particular, we consider the interpolation and integration issues. In order to enforce essential boundary conditions, the concept of primitive and enrichment function (Chen *et al.* 2003) is used. To start with, we employ Lagrange polynomials in order to construct the primitive functions. However, whilst Lagrange polynomials work well for smaller orders of polynomial reproduction ($p \leq 2$), oscillations are observed in the shape functions as p increases. Accordingly, for higher consistency, we use interpolating (Deslauriers-Dubuc) wavelet basis as the primitive function. A conformal knot-grid integration scheme is also proposed such that the integrals appearing in the weak form are (numerically) integrated over a grid formed by the knot vectors. Since B-spline basis functions are compactly supported between knot points ($N_{i,p}(\xi) = 0 \forall \xi \notin [\xi_i, \xi_{i+p+1})$ where $N_{i,p}(\xi)$ is the B-spline basis function of degree p defined over the knot vector $\Xi = \{\xi_1, \xi_2, \xi_3, \dots, \xi_{n+p+1} | \xi_i \in \mathbb{R}\}$ and n is the number of basis functions), supports of these basis functions always remain aligned with the grid formed by knot vectors. Consequently the non-conformability owing to the misalignment of support domains and background mesh is effortlessly bypassed. Finally we illustrate the numerical performance of the proposed method in the context of weak solutions of a few boundary value problems of relevance in solid mechanics.

While $a \otimes b$ indicates the standard tensor product of two vectors, $a \cdot b$ indicates the dot product and $a \times b$ the cross product of a and b . For convenience, the multi-index notation is adopted throughout this article. Thus defining

$\alpha = (\alpha_1, \alpha_2, \dots, \alpha_n)$ (with $n > 0$) to be an n -tuple of non-negative integers α_j , α is referred to as the multi-index and its length is defined as $|\alpha| = \sum_{i=1}^n \alpha_i$. The α^{th} (Fréchet) derivative of the function $u(x)$ is expressed as $D^\alpha u(x) = \partial_{x_1}^{\alpha_1} \partial_{x_2}^{\alpha_2} \dots \partial_{x_n}^{\alpha_n} u(x)$. We define $\alpha! = \alpha_1! \alpha_2! \dots \alpha_n!$ and $x^\alpha = x_1^{\alpha_1} x_2^{\alpha_2} \dots x_n^{\alpha_n}$. The rest of the paper is organized as follows. In sections 2, the piecewise NPMM is briefly outlined. Various aspects of interpolation and numerical integration are discussed respectively in sections 3 and 4. A few test cases are provided in section 5 to bring forth the efficacy of the proposed scheme. Conclusions are drawn in section 6.

2 The Piecewise NPMM

Consider an open and bounded domain $\Omega \subset \mathbb{R}^n$ with a Lipschitz continuous boundary $\partial\Omega \subset \mathbb{R}^{n-1}$. We denote by $\Omega_c = \Omega \cup \partial\Omega$ the closure of Ω . The construction of piecewise NPMM shape functions involves three main steps described below.

2.1 Construction of the Geometric Map

In the FEM, a major portion of the computational time is consumed in modeling and discretization of the domain geometry. It is then desirable to have a less costly representation of a complicated domain with the added requirement that, whenever required, the original geometry can be reproduced precisely. NURBS is a mathematical tool that provides a parametric representation of both analytic and free-form surfaces. It is generally defined by its order, control points, weights associated with control points and knot vectors (see Piegl and Tiller 1995 for details of B-spline and NURBS).

In an effort to exploit the parametric representation of the original geometry via NURBS in engineering analysis, Shaw and Roy (2007b) have recently proposed the NPMM. Here a parametric domain $\overline{\Omega} = [0, 1]^n$ (n denotes the physical dimension of the domain $\Omega_c = \Omega \cup \partial\Omega$) is so defined that there is a local bijection $F : \overline{\Omega} \rightarrow \Omega_c$ (figure 1). The transformation F , called the geometric map, is constructed through NURBS.

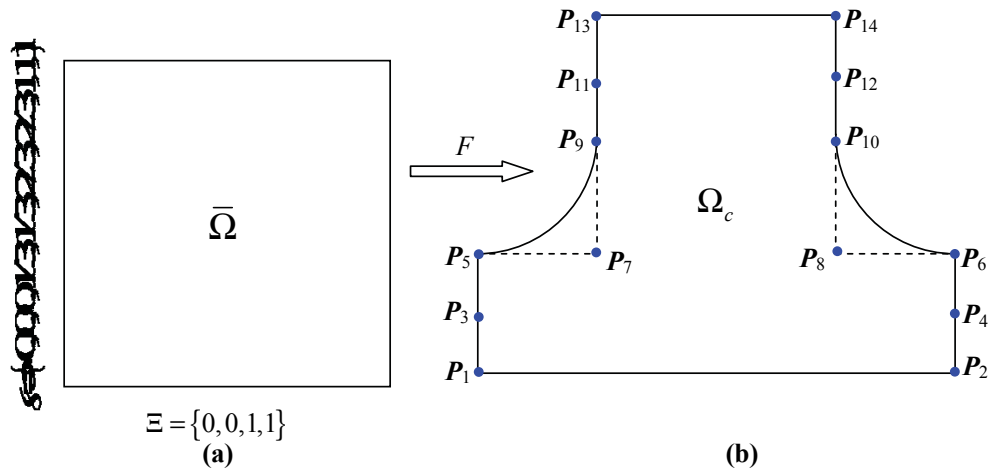


Figure 1: (a) Parametric domain and knot vectors; (b) physical domain and control points $\{P_i\}_{i=1}^{14}$

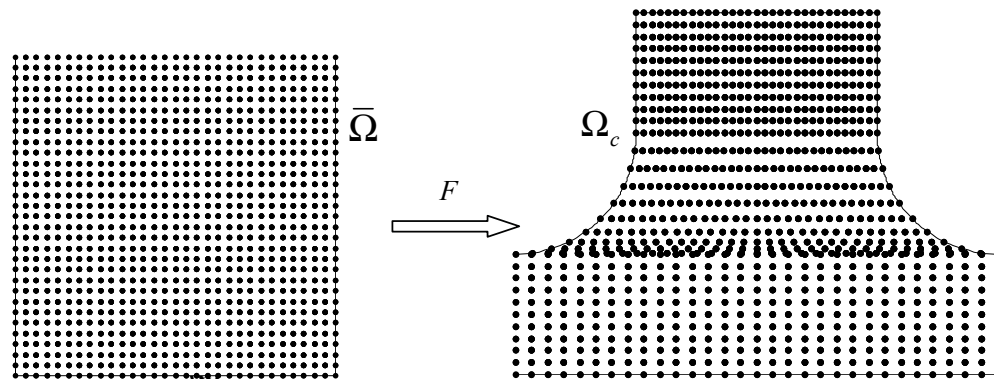


Figure 2: (a) Discretization $\{\bar{x}_i\}_{i=1}^{N_p} \subset \bar{\Omega}$ of the parametric domain; (b) corresponding discretization $\{x_i\}_{i=1}^{N_p} \subset \Omega_c$ of the physical domain

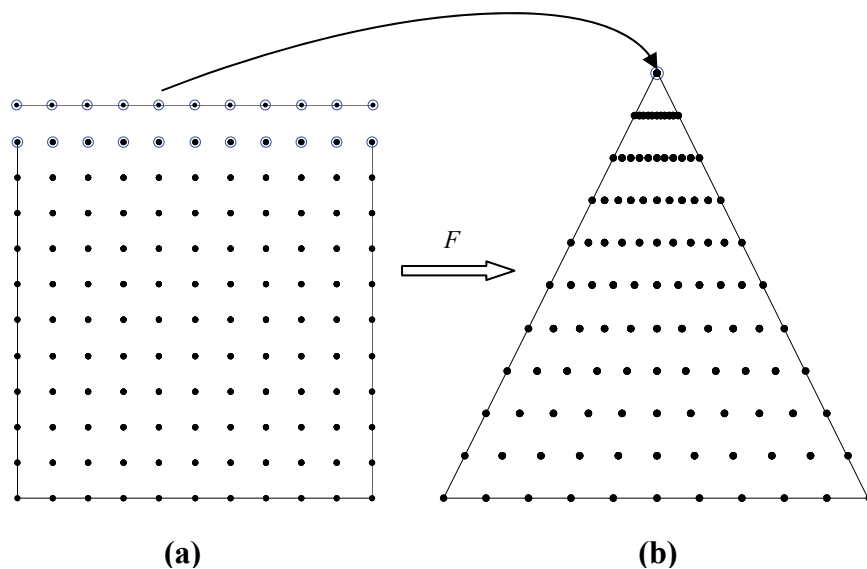


Figure 3: A triangular domain where the geometric map is not one-to-one; (a) discretization of the parametric space; (b) projection of the discretized parametric space on the physical space

Given F , the parametric domain $\bar{\Omega}$ is discretized by a set of grid points $\{\{\bar{x}_i\}_{i=1}^{N_p}\} \subset \bar{\Omega}$ (figure 2a) and the corresponding discretization $\{\{x_i\}_{i=1}^{N_p}\} \subset \Omega_c$ of the physical domain (figure 2b) is uniquely obtained via F . Then the shape function and its derivatives are so constructed over $\bar{\Omega}$ that polynomial reproduction and interpolation properties are satisfied over Ω_c and the geometric map F is simultaneously preserved.

The NPMM provides a relief from several computational pitfalls (e.g. dealing with a complicated geometry, choosing an optimal support size of the window function, choosing a conformal background mesh for accurate integration etc.) present in many other mesh-free methods. Nevertheless, bijective geometric maps may not exist for many (probably most) geometrical objects of practical importance (see figure 3). This imposes a severe restriction on the applicability of the NPMM and the situation may be sharply contrasted with the universality of the FEM.

In order to remove this restricted applicability and further generalize the method, we consider a piecewise form of the NPMM wherein the domain Ω_c is decomposed into N^e simply connected subdomains (element patches) $\{\Omega_c^e\}_{e=1}^{N^e}$ such that the following conditions hold.

1. Ω_c^e is closed and has a non-empty interior Ω^e
2. $\Omega_c = \bigcup_{e=1}^{N^e} \Omega_c^e$
3. $\Omega_c^i \cap \Omega_c^j = \emptyset$ for $i \neq j$ where Ω_c^j is the interior of Ω_c^j
4. There is a bijection $F^e : \bar{\Omega}^e \rightarrow \Omega_c^e$ for $\forall e \in [1, N^e]$ where $\bar{\Omega}^e = [0, 1]^n \subset \mathbb{R}^n$ is the parametric element associated with Ω_c^e .

For further illustration, consider a triangular domain shown in figure 4a. The domain Ω_c is decomposed (Figure 4b) into three ($N^e = 3$) element patches $\{\Omega_c^e\}_{e=1}^3$. Now, for each Ω_c^e , define a parametric element $\bar{\Omega}^e = [0, 1]^n \subset \mathbb{R}^n$ such that the image of any point $\bar{x} \in \bar{\Omega}^e$ in Ω_c^e may be obtained

as:

$$x = \sum_{i=1}^{N_{CP}^e} R_{i,p}^{eg}(\bar{x}) P_i^e \forall x \in \Omega_c^e \quad (1)$$

Here $R_{i,p}^{eg}(\bar{x})$ are the NURBS basis functions, $\{P_i^e\}_{i=1}^{N_{CP}^e}$ is a set of control points and N_{CP}^e is the number of control points associated with Ω_c^e (cardinality of the set). Equation (1) provides the geometric map $F^e : \bar{\Omega}^e \rightarrow \Omega_c^e$. For all Ω_c^e , $e \in [1, 3]$, NURBS basis functions $R_{i,p}^{eg}(\bar{x})$ are constructed over the knot space $\Xi^e \times \Upsilon^e \subset [0, 1]^2$ with two B-spline basis functions over the real line defined over $\Xi^e = \{0, 0, 1, 1\}$ and $\Upsilon^e = \{0, 0, 1, 1\}$.

In order to formalize the procedure within a more general setting, now consider a non-simply connected domain shown in figure 5a. The domain is decomposed (figure 5b) into 4 ($N^e = 4$) element patches $\{\Omega_c^e\}_{e=1}^4$ such that there exist a bijection $F^e : \bar{\Omega}^e \rightarrow \Omega_c^e$, for $e \in [1, 4]$.

Once the geometric map is obtained, each element patch may be discretized separately by transforming the discretization of its parametric domain to the physical domain. However, before we progress further, a few important issues related to the numbering system and the compatible domain decomposition criteria need to be put in place.

2.1.1 The Numbering System

The numbering system that we have presently adopted is shown in figure 6.

2.1.2 Control Vertices, Control Edges and Control Faces

If the parametric domain $\bar{\Omega}^e \subset \mathbb{R}^n$ is considered as a polytope, then the images of the polytope vertices, polytope edges and polytope faces in the physical domain are referred to as control nodes, control edges and control faces respectively. In figure 4, for instance, $\{1, 2, 5, 4\}$, $\{2, 3, 6, 5\}$ and $\{5, 6, 7, 4\}$ are the control vertex numbers; $\{1-2, 2-5, 5-4, 4-1\}$, $\{2-3, 3-6, 6-5, 5-2\}$ and $\{5-6, 6-7, 7-4, 4-5\}$ are the control edge numbers for elements Ω_c^1 , Ω_c^2 and Ω_c^3 respectively. Similarly, $\{6, 5, 1, 2\}$, $\{3, 7, 6, 2\}$,

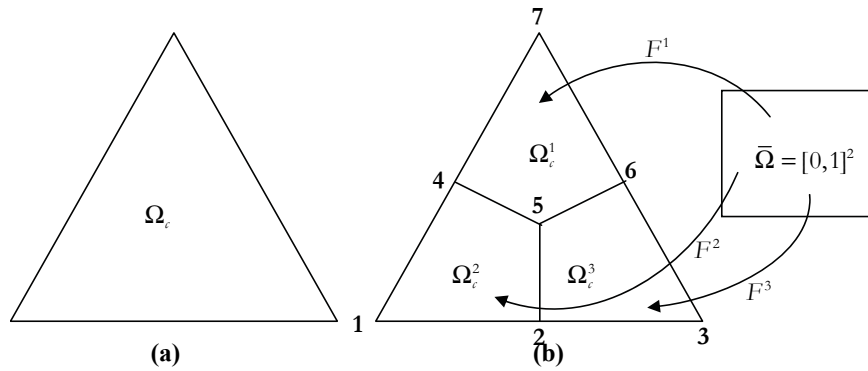


Figure 4: (a) Physical domain; (b) the same is decomposed into 3 sub-domains (element patches) Ω_c^1 , Ω_c^2 and Ω_c^3

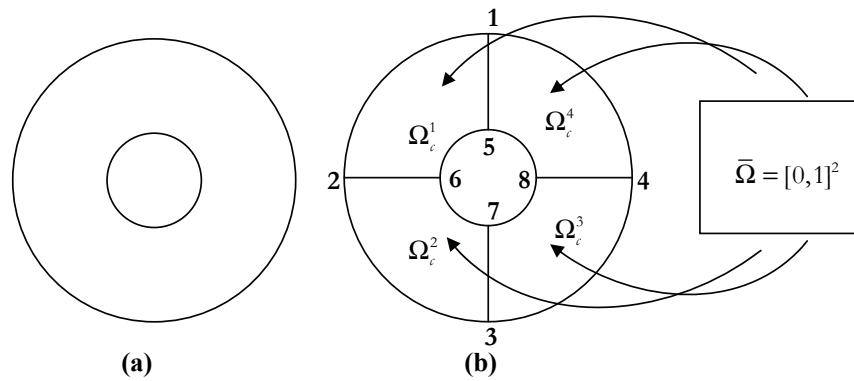


Figure 5: (a) Physical domain; (b) the same is decomposed into 4 element patches

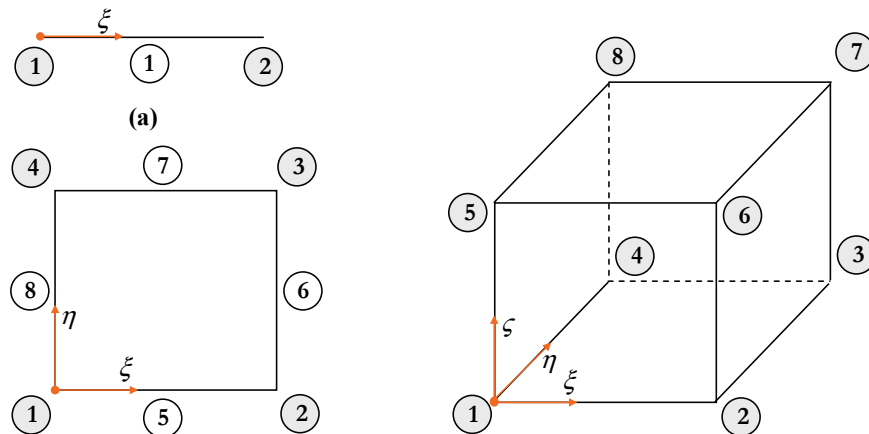


Figure 6: (a) Numbering system for different parametric domains; (a) line $\bar{\Omega} = [0, 1]$; (b) plane $\bar{\Omega} = [0, 1]^2$ and (c) solid $\bar{\Omega} = [0, 1]^3$ (see Table 1 for edge and face numbering for solid)

Table 1: Edge and surface numbering for parametric domain in \mathbb{R}^3

Edge		Surface	
Edge ID	Node number	Surface ID	Node number
9	1-2	21	1-2-3-4
10	2-3	22	1-2-6-5
11	3-4	23	2-3-7-6
12	4-1	24	3-4-8-7
13	5-6	25	4-1-5-8
14	6-7	26	5-6-7-8
15	7-8		
16	8-5		
17	1-5		
18	2-6		
19	3-7		
20	4-8		

$\{3, 4, 8, 7\}$ and $\{8, 4, 1, 5\}$ are the control vertex numbers and $\{6-5, 5-1, 1-2, 2-6\}$, $\{3-7, 7-6, 6-2, 2-3\}$, $\{3-4, 4-8, 8-7, 7-3\}$ and $\{8-4, 4-1, 1-5, 5-8\}$ are the control edge numbers for element patches Ω_c^1 , Ω_c^2 , Ω_c^3 and Ω_c^4 respectively for the physical domain shown in figure 5.

2.2 Compatible Domain Decomposition

We define:

$$\mathfrak{S}^e = \{i \in [1, N^e] : \Omega_c^e \cap \Omega_c^i \neq \emptyset\} \quad (2)$$

Now let V^e , E^e and F^e respectively denote the set of control vertices, control edges and control faces associated with Ω_c^e . Then the sub-domain Ω_c^e is said to be compatible with respect to $\{\Omega_c^i\}_{i \in \mathfrak{S}^e}$ if it satisfies at least one of the following conditions:

1. $V^e \cap V^i \subseteq \Omega_c^e \cap \Omega_c^i$, $i \in \mathfrak{S}^e$
2. $E^e \cap E^i \subseteq \Omega_c^e \cap \Omega_c^i$, $i \in \mathfrak{S}^e$
3. $F^e \cap F^i \subseteq \Omega_c^e \cap \Omega_c^i$, $i \in \mathfrak{S}^e$

The implication of the above compatibility conditions is as follows. If any two element patches intersect, then the control vertex, control edge and control face of one element patch will intersect respectively with control vertex, control

edge and control face of another. To make matters clearer, a typically incompatible domain decomposition and a couple of typically compatible ones are shown in figure 7.

2.3 Discretization

We discretize the parametric domain $\bar{\Omega}^e$ by the set of grid points $\{\{\bar{x}_i^e\}_{i=1}^{N_p^e}\} \subset \bar{\Omega}^e$ and denote $\{\{x_i^e\}_{i=1}^{N_p^e}\}$ to be the corresponding image set in Ω_c^e obtained via the transformation F^e (equation 1). Figures 8 and 9 show the discretization of $\bar{\Omega}^e$ and the corresponding image in Ω_c^e for the domains shown in figures 4 and 5 respectively.

2.4 The Piecewise NPM Approximation

Let $u(x)$, $x \in \mathbb{R}^n$ be an L^∞ (sufficiently smooth) function defined on an open set containing Ω_c and $\{\{x_i\}_{i=1}^{N_p}\} \subset \Omega_c$ be a discretization of the physical domain Ω_c . This enables us to define the set of discretized (point-wise) function values $\{u_i \triangleq u(x_i)\}_{i=1}^{N_p}$. Consider any point $x \in \Omega_c^e$ with $\bar{x} \in \bar{\Omega}^e$ denoting the pre-image of x . Let $\mathfrak{K}^e \subset \mathbb{R}^n$ be the knot space associated with $\bar{\Omega}^e$ and $R_{i,p+1}^e(\bar{x})$ be the NURBS basis function of degree $p+1$ (required to achieve p^{th} order consistency; see section 3) defined over \mathfrak{K}^e . Define $S^e(\bar{x})$ as:

$$S^e(\bar{x}) = \{i : R_{i,p+1}^e(\bar{x}) > 0\}. \quad (3)$$

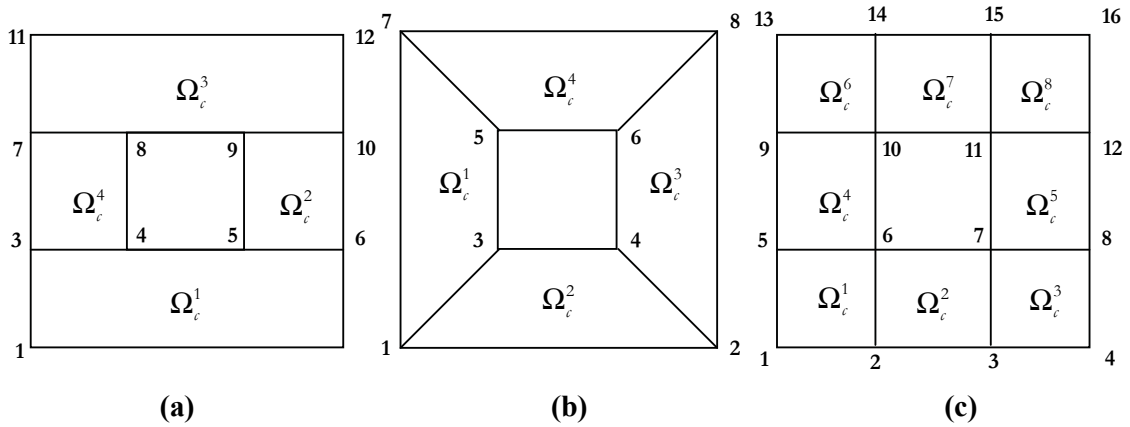


Figure 7: (a) Incompatible domain decomposition; (b) – (c) compatible domain decomposition

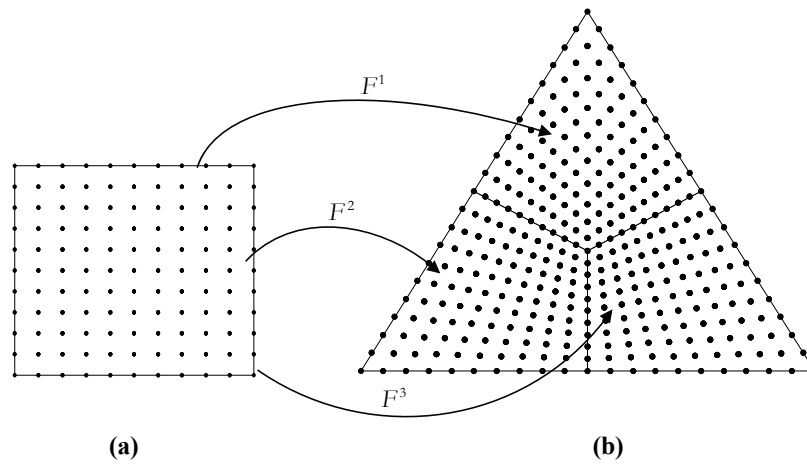


Figure 8: (a) Discretization of the parametric domain $\bar{\Omega}^e = [0, 1]^2$; (b) projection in the physical domain $\Omega_c \subset \mathbb{R}^2$

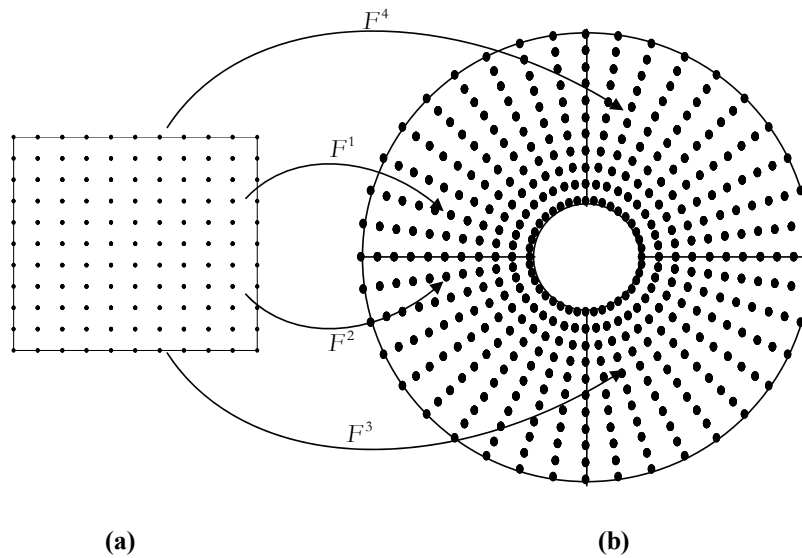


Figure 9: (a) Discretization of the parametric domain $\bar{\Omega}^e = [0, 1]^2$; (b) projection in the physical domain $\Omega_c \subset \mathbb{R}^2$

Shaw and Roy (2008) have demonstrated that, while constructing the parametric mesh-free shape function, we need to choose \mathfrak{N}^e properly in order to satisfy the regularity condition. This may be achieved by taking a few knots outside the domain $\bar{\Omega}^e$. For example, in the one-dimensional ($n = 1$) case, one may use $\mathfrak{N}^e \subset [-\varepsilon_x, 1 + \varepsilon_x]$. Similarly, we have, for higher dimensions:

$$\mathfrak{N}^e \subset [-\varepsilon_x, 1 + \varepsilon_x] \times [-\varepsilon_y, 1 + \varepsilon_y] \text{ for } n = 2$$

and

$$\mathfrak{N}^e \subset [-\varepsilon_x, 1 + \varepsilon_x] \times [-\varepsilon_y, 1 + \varepsilon_y] \times [-\varepsilon_z, 1 + \varepsilon_z] \\ \text{for } n = 3.$$

Here ε_x , ε_y and ε_z are parameters to be so chosen that

$$\text{card}(S^e(\bar{x})) \geq \frac{(p+n)!}{p!n!} \quad \forall \bar{x} \in \bar{\Omega}^e \quad (4)$$

where $\text{card}(\cdot)$ denotes the cardinality of the set (\cdot) . Towards maintaining a simple exposition with the least diversion, we presently assume a uniform particle distribution over $\bar{\Omega}^e$ and also take $\varepsilon_x = \varepsilon_y = \varepsilon_z = \varepsilon$. Now define two scaled parametric spaces $\tilde{\Omega}^e$ and $\hat{\Omega}^e$ (figure 10a) obtained respectively by the geometric expansion and contraction of the parametric space $\bar{\Omega}^e$ as:

$$\tilde{\Omega}^e = [-\varepsilon, 1 + \varepsilon]^n \subset \mathbb{R}^n \quad (5)$$

$$\hat{\Omega}^e = [\varepsilon, 1 - \varepsilon]^n \subset \mathbb{R}^n \quad (6)$$

We also define $\tilde{\Omega}_c^e$ and $\hat{\Omega}_c^e$ as the projections of $\tilde{\Omega}^e$ and $\hat{\Omega}^e$ respectively onto the physical domain (figure 10b). Figures 11a through 11d show projections of the scaled parametric domains in the physical domain for each element patch corresponding to the examples shown in figures 4 and 5.

Depending on the nodal coordinates, we may have following two cases.

Case 1:

If $x \in \hat{\Omega}_c^e$ ($\Rightarrow \bar{x} \in \hat{\Omega}^e$) then it does not have any interaction (in terms of approximations of the field variables at that point getting affected by the shape function corresponding to another

point) with other element patches and the piecewise NPMM shape function simply reduces to the parametric mesh-free shape function (Shaw and Roy 2008) applied over Ω_c^e . The reproducing condition may be written as:

$$\sum_{i=1}^{N_p} \Psi_i(x) x_i^\alpha = x^\alpha, \quad |\alpha| \leq p \\ \Rightarrow \sum_{i=1}^{N_p} \Psi_i(x) H(x - x_i) = H(0) \quad (7)$$

$H(x) = \{x^\alpha\}_{|\alpha| \leq p}^T$ is a set of monomial basis functions and α is the multi-index. From equation (7), we may write:

$$x = \sum_{i=1}^{N_{CP}} R_{i,p}^{eg}(\bar{x}) P_i^e \quad (8)$$

$$x - x_i = \sum_{k=1}^{N_{CP}} R_{k,q}^{eg}(\bar{x}) P_k^e - \sum_{k=1}^{N_{CP}} R_{k,q}^{eg}(\bar{x}_i^e) P_k^e$$

\Rightarrow

$$H(x - x_i) = \sum_{k=1}^{N_{CP}} [R_{k,q}^{eg}(\bar{x}) - R_{k,q}^{eg}(\bar{x}_i^e)] P_k^e = \bar{H}(\bar{x}_i^e, \bar{x}) \quad (9)$$

Now $\Psi_i(x)$ may be written as:

$$\Psi_i(x) = \bar{H}^T(\bar{x}_i^e, \bar{x}) b(x) R_{i,p+1}^e(\bar{x}) \quad (10)$$

$b(x)$ is the vector of unknown coefficients. Using equations (7) and (10), we may write:

$$\Rightarrow \sum_{i=1}^{N_p} \bar{H}(\bar{x}_i^e, \bar{x}) b(x) R_{i,p+1}^e(\bar{x}) \bar{H}(\bar{x}_i^e, \bar{x}) = H(0) \quad (11)$$

$$\Rightarrow \bar{M}(x) b(x) = H(0) \quad (12)$$

$$\Rightarrow b(x) = \bar{M}^{-1}(x) H(0) \quad (13)$$

$\bar{M}(x)$ is the parametric moment matrix given by:

$$\bar{M}(x) = \sum_{i=1}^{N_p} \bar{H}(\bar{x}_i^e, \bar{x}) \bar{H}^T(\bar{x}_i^e, \bar{x}) R_{i,p+1}^e(\bar{x}) \quad (14)$$

Using equations (10), (11) and (13), the parametric mesh free shape function $\Psi_i(\bar{x})$ may be expressed as:

$$\Psi_i(x) = H^T(0) M^{-1}(\bar{x}) \bar{H}(\bar{x}_i^e, \bar{x}) R_{i,p+1}^e(\bar{x}), \\ i \in S^e(\bar{x}) \quad (15)$$

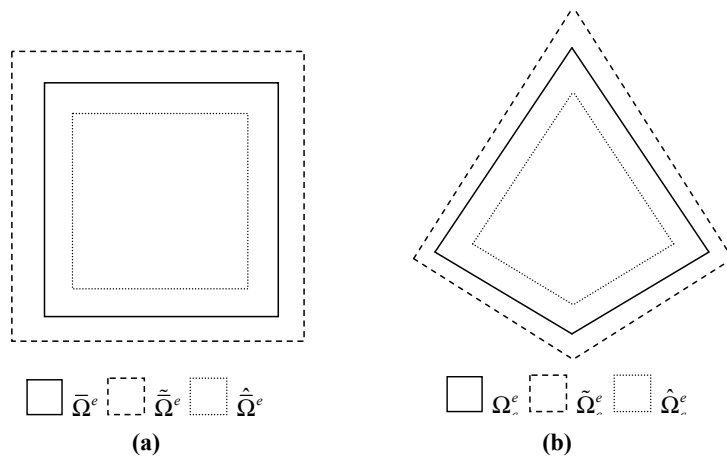


Figure 10: (a) Scaled parametric spaces; (b) projections on the physical domain

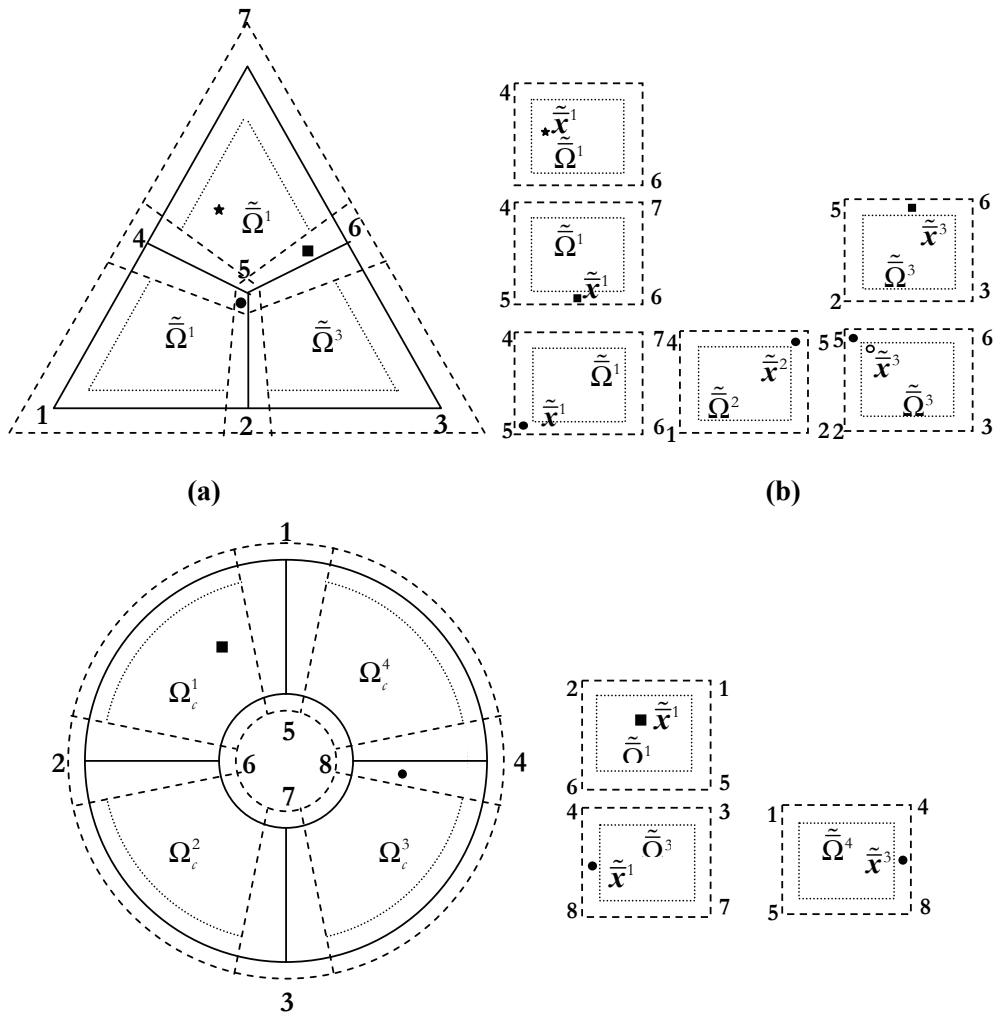


Figure 11: (a), (c) Projection of the scaled parametric domain on the physical domain; (b), (d) pre-image of any point x in the corresponding parametric space.

Similarly derivatives of the parametric basis function may be obtained based on the premise that the β^{th} derivative of the basis function would exactly reproduce the β^{th} derivative of an arbitrary element of the space P_p of polynomials of degree $p \geq |\beta|$. Thus, following Shaw and Roy (2007b), the β^{th} derivative of the parametric mesh-free basis function may be obtained as:

$$\begin{aligned} \Psi_i^{(\beta)}(x) = & \\ (-1)^{|\beta|} H^{T(\beta)}(0) M^{-1}(\bar{x}) \bar{H}(\bar{x}_i, \bar{x}) R_{i,p+1}^e(\bar{x}), & \\ i \in \mathcal{S}^e(\bar{x}) & \quad (16) \end{aligned}$$

Case 2:

If $x \in \tilde{\Omega}_c^e \setminus \hat{\Omega}_c^e (\Rightarrow \bar{x} \in \tilde{\Omega}^e \setminus \hat{\Omega}^e)$ then the piecewise NPMM shape function at $x \in \Omega_c^e$ will have interactions with all other element patches overlapping Ω_c^e . As the first step in capturing such interactions, we define:

$$\Gamma_i^e = \{j \in [1, N_p] : x_i \in \Omega_c^e \cap \Omega_c^j\} \quad (17)$$

Let $\tilde{x}^j \in \tilde{\Omega}^j, j \in \mathcal{S}^e$, be the pre-image of x (see figure 11). The procedure for finding $\tilde{x}^j \in \tilde{\Omega}^j$ is discussed in section 2.4. Now the NURBS approximation of any function $u(x)$ may be written as:

$$u^a(x) = \sum_{j \in \mathcal{S}^e(\bar{x})} \sum_{i \in \mathcal{S}^j(\tilde{x}^j)} w_i R_{i,p}^j(\tilde{x}^j) u_i \quad (18)$$

where

$$w_i = \frac{1}{\text{card}(\Gamma_i^e)}. \quad (19)$$

Since NURBS does not reproduce polynomials beyond first order, we introduce a correction function into the approximation. Then the piecewise NPMM approximation of the function $u(x)$ may be written as:

$$u(x) = \sum_{j \in \mathcal{S}^e(\bar{x})} \sum_{i \in \mathcal{S}^j(\tilde{x}^j)} C_i(x) \bar{R}_{i,p}^j(\tilde{x}^j) u_i \quad (20)$$

where

$$\bar{R}_{i,p}^j(\tilde{x}^j) = w_i R_{i,p}^j(\tilde{x}^j) \quad (21)$$

The correction term $C_i(x)$ may be obtained via the following reproducing condition:

$$x^\alpha = \sum_{j \in \mathcal{S}^e(\bar{x})} \sum_{i \in \mathcal{S}^j(\tilde{x}^j)} C_i(x) \bar{R}_{i,p}^j(\tilde{x}^j)(x_i)^\alpha \quad (22)$$

Putting $C_i(x) = H^T(x - x_i)b(x)$ in equation (22), we arrive at the following identity:

$$x^\alpha = \sum_{j \in \mathcal{S}^e(\bar{x})} \sum_{i \in \mathcal{S}^j(\tilde{x}^j)} H^T(x - x_i)b(x) \bar{R}_{i,p}^j(\tilde{x}^j)(x_i)^\alpha \quad (23)$$

$H^T(x - x_i)$ is the set of monomial basis and $b(x)$ is the vector of unknown coefficients. Now equation (23) may be written as:

$$\begin{aligned} \sum_{j \in \mathcal{S}^e(\bar{x})} \sum_{i \in \mathcal{S}^j(\tilde{x}^j)} H^T(x - x_i)b(x) \bar{R}_{i,p}^j(\tilde{x}^j) H(x - x_i) & \\ = H(0) & \quad (24) \end{aligned}$$

$$\begin{aligned} \Rightarrow \sum_{j \in \mathcal{S}^e(\bar{x})} \sum_{i \in \mathcal{S}^j(\tilde{x}^j)} H(x - x_i) H^T(x - x_i) \bar{R}_{i,p}^j(\tilde{x}^j) b(x) & \\ = H(0) & \quad (25) \end{aligned}$$

$$\Rightarrow M_{NSFEM}(x)b(x) = H(0) \quad (26)$$

$$\Rightarrow b(x) = M_{NSFEM}^{-1}(x)H(0) \quad (27)$$

where $M_{NSFEM}(x)$ is the NSFEM moment matrix given by:

$$\begin{aligned} M_{NSFEM}(x) = & \\ \sum_{j \in \mathcal{S}^e(\bar{x})} \sum_{i \in \mathcal{S}^j(\tilde{x}^j)} H(x - x_i) H^T(x - x_i) \bar{R}_{i,p}^j(\tilde{x}^j) & \quad (28) \end{aligned}$$

Similarly the β^{th} derivative of the piecewise NPMM approximation may be written as:

$$u^\beta(x) = \sum_{j \in \mathcal{S}^e(\bar{x})} \sum_{i \in \mathcal{S}^j(\tilde{x}^j)} H^T(x - x_i) b^\beta(x) \bar{R}_{i,p}^j(\tilde{x}^j) u_i \quad (29)$$

$b^\beta(x)$ is the coefficient vector for derivative calculation and may be obtained from the derivative reproduction condition as:

$$b^{(\beta)}(x) = (-1)^{|\beta|} M_{NSFEM}^{-1}(x) H^{T(\beta)}(0) \quad (30)$$

where $M_{NSFEM}(x)$ is the moment matrix given by equation (28) and $H^{(\beta)}$ is the β^{th} derivative of the monomial basis. We emphasize that the ability of the shape functions (in case 2) to reproduce polynomials up to a desired degree plays a crucial role in maintaining the globally smooth nature (to any desired order) of the shape functions, even across the boundaries of the patches.

2.5 Local Parametric Assembly (LPA)

The concept of local parametric assembly (LPA) is introduced in the doctoral thesis of Shaw (2007) in order to find the parametric coordinate $\tilde{x}^e \in \tilde{\Omega}^j$ corresponding to the physical coordinate x for each sub-domain Ω_c^j where $j \in \mathfrak{S}^e$. The parametric assembly of any two sub-domains is the equivalent assembly of the corresponding sub-domains in their parametric spaces. For example, consider once more the triangular domain shown in figure 4. Figure 12 shows the numbering of the control nodes and control edges for each sub-domain with respect to their parametric spaces. The local parametric assemblies of Ω_c^1 with Ω_c^2 and Ω_c^3 are shown in figures 13a and 13b respectively.

Once the local parametric assembly of Ω_c^e with $\tilde{\Omega}^j, j \in \mathfrak{S}^e$, is identified, $\tilde{x}^e \in \tilde{\Omega}^j$ may be obtained as the coordinate of $\bar{x} \in \tilde{\Omega}^e$ with respect to $\tilde{\Omega}^j$. For example, in figure 13, the coordinates of $\bar{x} = (\xi, \eta) \in \tilde{\Omega}^1$ (indicated by a black dot) with respect to $\tilde{\Omega}^2$ and $\tilde{\Omega}^3$ may be obtained as,

$$\tilde{x}^2 = (\xi^2, \eta^2) = (1 - \eta, 1 + \xi)$$

$$\tilde{x}^3 = (\xi^3, \eta^3) = (1 + \xi, 1 + \eta)$$

For each local parametric assembly, we assign a number (LPA ID) according to the following scheme.

For node-node assembly ($n \geq 1$):

LPA ID = Control node number of Ω_c^e – Control node number of Ω_c^j

For edge-edge assembly ($n \geq 2$):

LPA ID = Control edge number of Ω_c^e – Control edge number of Ω_c^j

For face-face assembly ($n \geq 3$):

LPA ID = Control face number of Ω_c^e – Control face number of Ω_c^j

Different parametric assemblies in one and two dimensions have been provided in (Shaw 2007).

3 The Interpolation

The piecewise NPMM shape function, discussed in section 2.3, does not satisfy the Kronecker delta property and fails to vanish at the essential boundaries. Therefore the imposition of essential boundary conditions is not as trivial as in the FEM. Shaw and Roy (2008) have proposed a couple of scheme viz. the point inverse method and another via Kriging, to bring in the interpolation property in the parametric mesh-free method. In the point inverse method, interpolation property is achieved by multiplying the basis functions by an inverse transformation. Though the method is quite straightforward, use of the inverse transformation induces the bandwidth of the discretized system to become larger than that obtainable through the basis without the nodal interpolation property. This increases the size of the influence domain and may even affect the accuracy of the solution, especially when the targeted response is spatially localized. In Kriging-based interpolation schemes, interpolating basis functions are obtained by minimizing the squared variance of the finite dimensional approximation with the reproduction property (of any desired level of consistency) as constraints. Though the reproduction and the interpolation properties are simultaneously achieved in the Kriging-based interpolation scheme, its use demands more computational effort due to the larger size (depends on the number of particles in the influence domain) of the coefficient matrix. Moreover, since we need to specify the support size of the semivariogram, the issue of choosing an optimal support size still remains.

In the context of the piecewise NPMM, we presently use the concept of primitive and enrichment functions (Chen *et al.* 2003) in order to enforce the essential boundary condition. The essence of the method is to use an arbitrary function, called the primitive function, that satisfies the Kronecker delta property at the boundary nodes (or wherever interpolation is required) and then an enrichment function is added to the prim-

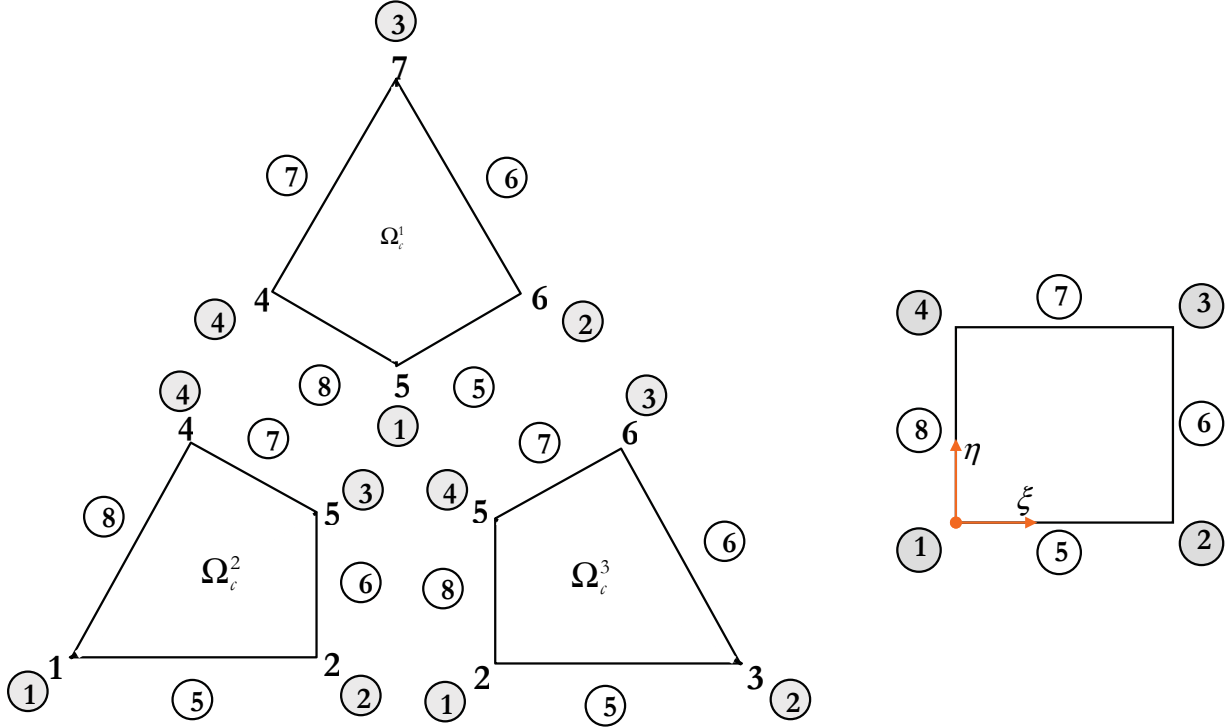


Figure 12: Control node and control edge numbers for each sub-domain for the triangular domain shown in figure 8

itive function in order to achieve the necessary consistency condition. Now mesh-free approximation of $u(x) \in C(\Omega_c)$ may be written as:

$$u^a(x) = \sum_{i=1}^{N_p} \Psi_i(x) u_i \quad (31)$$

$\Psi_i(x)$, along with its constituent basis function may be written as:

$$\Psi_i(x) = \tilde{\Psi}_i(x) + \bar{\Psi}_i(x)$$

where $\tilde{\Psi}_i(x)$ is the primitive functions that satisfies the Kronecker delta property and $\bar{\Psi}_i(x)$ is the enrichment functions. $\bar{\Psi}_i(x)$ may be obtained by satisfying the p^{th} order reproducing condition:

$$\sum_{i=1}^{N_p} [\tilde{\Psi}_i(x) + \bar{\Psi}_i(x)] x_i^\alpha = x^\alpha, \quad |\alpha| \leq p \quad (32)$$

$$\Rightarrow \sum_{i=1}^{N_p} [\tilde{\Psi}_i(x) + \bar{\Psi}_i(x)] H(x - x_i) = H(0) \quad (33)$$

$$\Rightarrow \sum_{i=1}^{N_p} \bar{\Psi}_i(x) H(x - x_i) = H(0) - \sum_{i=1}^{N_p} \tilde{\Psi}_i(x) H(x - x_i)$$

(34)

Following equation (33) and section 2.3 the interpolating basis may be obtained as:

Case 1: $x \in \hat{\Omega}_c^e (\Rightarrow \bar{x} \in \hat{\Omega}^e)$

$$\Psi_i(x) = \left[H(0) - \sum_{i=1}^{N_p} \tilde{\Psi}_i(x) \bar{H}(\bar{x}_i^e, \bar{x}) \right]^T M^{-1}(\bar{x}) \bar{H}(\bar{x}_i^e, \bar{x}) R_{i,p+1}^e(\bar{x}), \quad i \in S^e(\bar{x}) \quad (35)$$

$$\Psi_i^{(\beta)}(x) = (-1)^{|\beta|} \left[H(0) - \sum_{i=1}^{N_p} \tilde{\Psi}_i(x) \bar{H}(\bar{x}_i^e, \bar{x}) \right]^{T(\beta)} (0) M^{-1}(\bar{x}) \bar{H}(\bar{x}_i^e, \bar{x}) R_{i,p+1}^e(\bar{x}), \quad i \in S^e(\bar{x}) \quad (36)$$

Case 2: $x \in \tilde{\Omega}_c^e \setminus \hat{\Omega}_c^e (\Rightarrow \bar{x} \in \tilde{\Omega}^e \setminus \hat{\Omega}^e)$

$$u(x) = \sum_{j \in S^e(\bar{x})} \sum_{i \in S^j(\bar{x}^j)} H^T(x - x_i) b(x) \bar{R}_{i,p}^j(\bar{x}^j) u_i \quad (37)$$

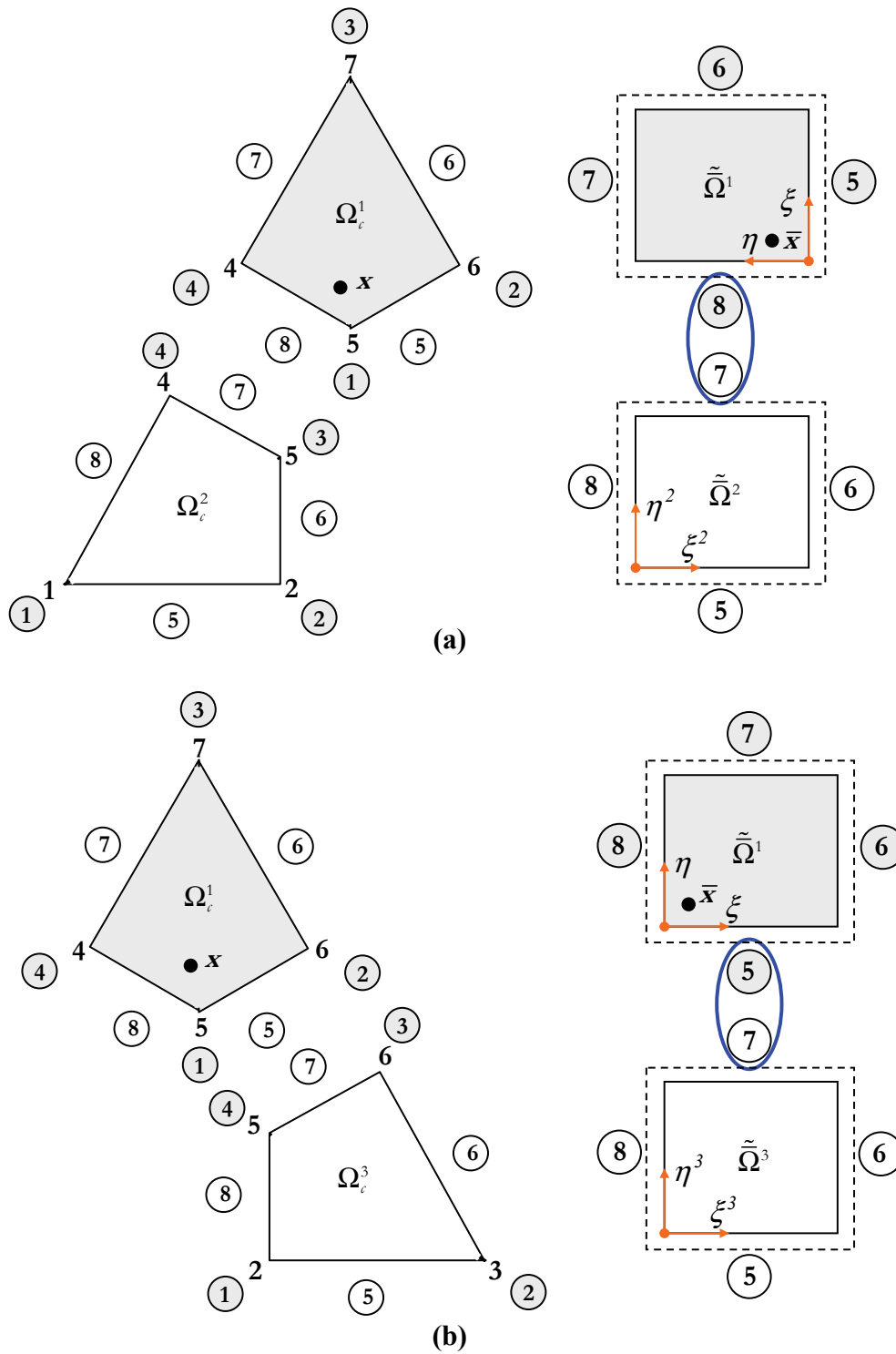


Figure 13: Local parametric assemblies (LPA) of Ω_c^1 with (a) Ω_c^2 and (b) Ω_c^3

$$b(x) = M_{NSFEM}^{-1}(x) \left[H(0) - \sum_{i=1}^{N_p} \tilde{\Psi}_i(x) \bar{H}(\bar{x}_i^e, \bar{x}) \right] \quad (38)$$

Similarly the β^{th} derivative of the piecewise NPMM approximation may be written as:

$$u^\beta(x) = \sum_{j \in \mathcal{S}^e(\bar{x})} \sum_{i \in \mathcal{S}^j(\bar{x}^j)} H^T(x - x_i) b^\beta(x) \bar{R}_{i,p}^j(\bar{x}^j) u_i \quad (39)$$

$b^\beta(x)$ is the coefficient vector for derivative calculation and may be obtained from the derivative reproduction condition:

$$b^{(\beta)}(x) = (-1)^{|\beta|} M_{NSFEM}^{-1}(x) \left[H(0) - \sum_{i=1}^{N_p} \tilde{\Psi}_i(x) \bar{H}(\bar{x}_i^e, \bar{x}) \right]^{T(\beta)} \quad (40)$$

In Chen *et al.* (2003), a cubic spline is used as the primitive function $\tilde{\Psi}_i(x)$. In order to satisfy the Kronecker delta property, the support size of $\tilde{\Psi}_i(x)$ is chosen very small (less than the smallest distance between two successive grid points over which the enrichment functions are defined) so that the supports do not cover any neighboring points. A major difficulty with this approach is as follows. As the number of discretization points increases (leading to progressively smaller support sizes of the primitive functions), solutions are likely to have spurious oscillations especially in the higher order derivatives. Presently, we first attempt using Lagrange polynomials in order to construct $\tilde{\Psi}_i(x)$. Numerical tests readily verify that even as Lagrange polynomials work well for smaller $p (\leq 2)$, spurious oscillations in the shape functions appear as p increases. For higher consistency, the interpolating (Deslauriers-Dubuc) wavelet basis appears to offer a good option as the primitive function. A brief description of the Deslauriers-Dubuc interpolating wavelet is provided in the Appendix A. However, for a more detailed account, we refer to (Donoho 1992).

3.0 Numerical Integration in the Piecewise NPMM

Methods based on any weak (e.g. Bubnov-Galerkin) formulation require (numerical) evalua-

tion of integrals. In the context of numerical integration to be performed during a weak implementation of the mesh-free method, we must account for two sources of difficulties/errors. Firstly, mesh-free shape functions and their derivatives are of more complex nature, especially at the support boundaries, than polynomial-like shape functions commonly used with the FEM. As reported in the literature, this appears to entail an (abnormally) larger number of integration points for sufficiently “accurate” evaluations of the integrals in the weak form (Belytschko *et al.* 1994). Use of such exceedingly high order quadrature rules not only violate the a-priori error estimates, but also lead to extremely high computational overhead vis-à-vis the FEM. Secondly, while evaluating the integrals in the weak form, a hidden cell structure (often called the background mesh) is employed in mesh-free methods. The background mesh is generally constructed independent of the particle distribution. In the process, there may be misalignments of supports of shape functions with respect to the integrations cells – an aspect that makes the method non-conforming (see figure 14). The non-conformability of support domains and the background mesh may lead to substantial numerical errors and thus affect the convergence of solutions (Dolbow and Belytschko 1999). Whilst the numerical difficulties arising out of the complicated nature of shape functions cannot possibly be bypassed, we can address, to a great extent, the issue of non-conformability by appropriately choosing cells for numerical integration. In the piecewise NPMM, this may, in particular, be accomplished by integrating the functional in the weak form over a grid formed by the knot vectors. B-spline basis functions are compactly supported between two (appropriately chosen) knot points and hence the support of B-spline basis functions is always aligned with the grid formed by such knot vectors. For further illustration, first consider a one dimensional domain $\bar{\Omega} \in \mathbb{R}$ discretized by $N_p = 9$ nodes as shown in figure 15. p^{th} degree B-spline basis functions are constructed over the knot vector $\Xi = \{\xi_1, \xi_2, \dots, \xi_{N_p+p+1}\}$. Suppose that the domain $\bar{\Omega}$ is divided uniformly into five integration cells (see figure 16). Figure 16 also shows two typi-

cal B-spline basis functions, defined over Ξ . We observe that the supports of B-spline basis functions do not coincide with the boundary of the integration cells (shown by “|” in figure 16a). On the other hand, if we take the grid formed by the knot vector as the set of integration cells (shown in figure 16b), then the supports of B-spline basis functions remain precisely aligned with the background mesh.

For an elucidation in the higher dimension, consider a domain $\bar{\Omega} \in \mathbb{R}^2$. The discretization and the background mesh, generally employed in the element free Galerkin method, and the grid formed by the knot-grid approach are shown in figure 17. We readily observe that, in contrast to the EFG, the support of the window function is perfectly aligned with the background mesh in the piecewise NPMM.

Even as the numerical integration using the knot-grid scheme makes the method conforming, we have observed through some numerical experiments that the accuracy of solutions may also get affected by the choice of knot positions. Uniform knot distribution over the parametric space (as shown in figures 18a and 19a) should be an obvious choice. However this may not always work, especially if the particle distribution does not follow a uniform grid structure. Our numerical experiments, some of which are reported in the following section, suggest that the knot-grid integration may work better if nodal points are chosen as knot points (see figures 18b and 19b).

Towards a numerical demonstration of the conformability of the piecewise NPMM, we consider Poisson's equation in two dimensions:

$$u_{,xx} + u_{,yy} = \frac{1}{2}(x^2 + y^2) - 1 \quad \text{in } \Omega = (-1, 1) \times (-1, 1) \quad (41a)$$

$$\text{with } u = x \text{ on } \partial\Omega \quad (41b)$$

The exact solution is:

$$u(x, y) = \frac{1}{4}(1 - x^2)(1 - y^2) + x \quad (42)$$

A detailed theoretical analysis of the proposed method (including an a-priori error estimate) is

still to be undertaken. However, given the globally smooth nature and boundedness of the piecewise NPMM shape functions, we presently use the following error estimate (Han and Meng 2001) in order to study the numerical convergence:

$$\|u - u^R\|_{L^2} \leq ch^{p+1} \quad (43)$$

$$\|u - u^R\|_{H^1} \leq ch^p \quad (44)$$

Here h is the spatial step size and u^R is the mesh-free solution of a second order elliptic boundary value problem with Dirichlet boundary conditions, $u \in H^{p+1}(\Omega_c)$ is the exact solution and $H^{p+1}(\Omega_c)$ is a Lebesgue (Sobolev) space with square integrable $(p+1)^{th}$ derivatives. In equation (34), the relative norms $\|\cdot\|_{L^2}$ and $\|\cdot\|_{H^1}$ are defined as:

$$\|u - u^R\|_{L^2} = \frac{\left(\int_{\Omega} (u - u^R) \cdot (u - u^R) d\Omega \right)^{1/2}}{\left(\int_{\Omega} u^2 d\Omega \right)^{1/2}} \quad (45)$$

$$\|u - u^R\|_{H^1} = \frac{\left(\int_{\Omega} \left\{ (u - u^R) \cdot (u - u^R) + (u' - u'^R) \cdot (u' - u'^R) \right\} d\Omega \right)^{1/2}}{\left(\int_{\Omega} (u^2 + u'^2) d\Omega \right)^{1/2}} \quad (46)$$

The weak solution of equation (40) is obtained with $N^e = 4$ and $p = 1$. A few h -convergence results in relative L_2 and H_1 error norms via quadrature rules of different orders are shown in figure 20. The optimum rate of convergence (2 in L_2 norm and 1 in H_1 norm for $p = 1$) is achieved even with a 2-point Gauss quadrature. The convergence rate remains about the same irrespective of the quadrature rule.

4 Numerical Examples

In this section, the proposed method is explored in the context of few boundary value problems

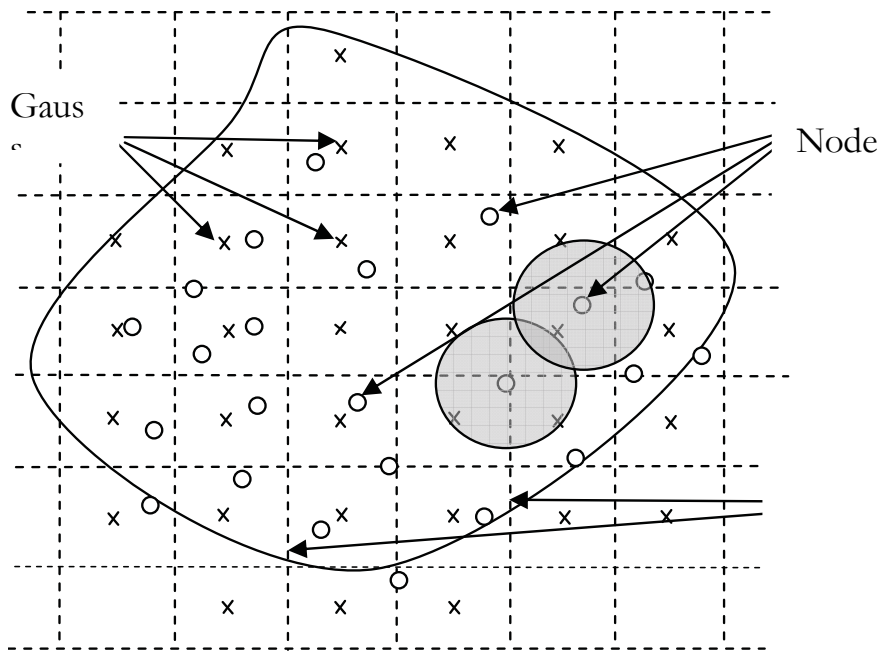


Figure 14: A typical discretization, support domains and background mesh

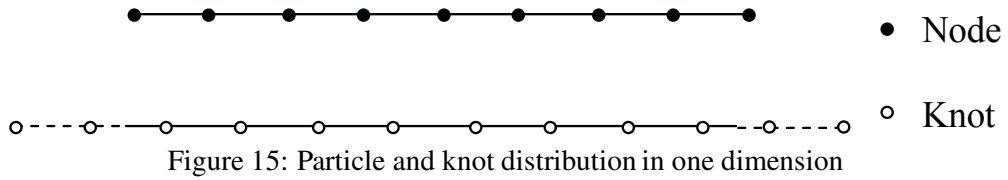


Figure 15: Particle and knot distribution in one dimension

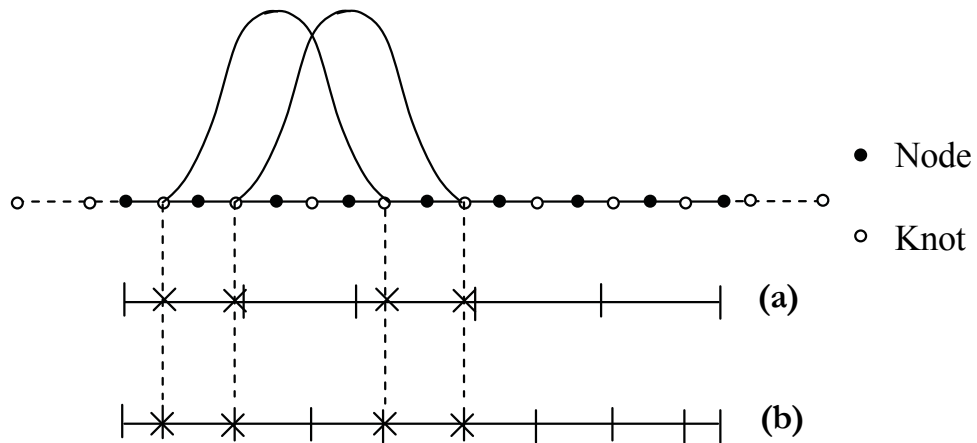


Figure 16: (a) Background mesh commonly used in mesh-free method; (b) knot-grid used as the background mesh in the piecewise NPMM

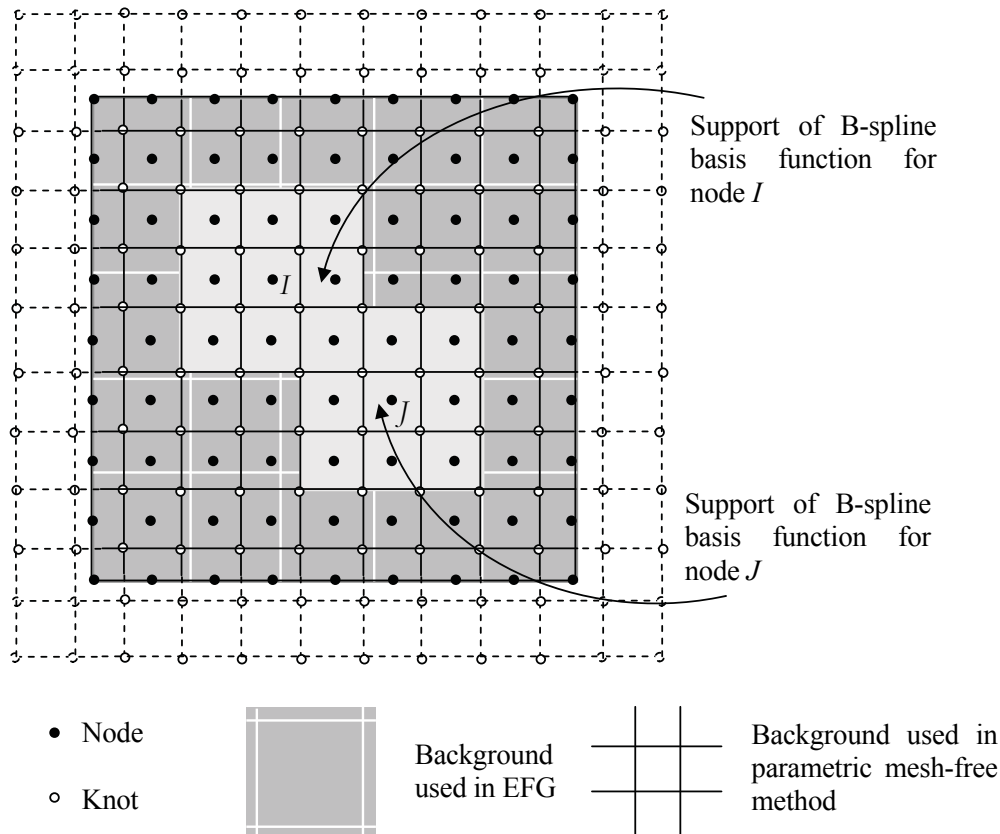


Figure 17: A typical discretization, support domains and background mesh (knot-grid) in the piecewise NPM

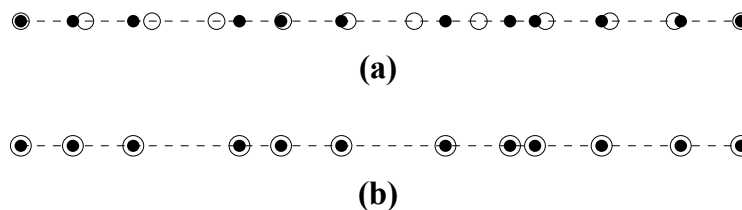


Figure 18: Typical node and knot distributions in the piecewise NPM in one dimension; (a) uniform knot vector irrespective of the particle distribution; (b) knot points and nodal points are taken the same

(of relevance in solid mechanics) with arbitrary domain geometries. In all the examples involving weak formulations, 2-point Gauss quadrature is used for numerical integration. Details of the geometric data (e.g. knot vectors, control points and the associated weights) for all the examples are provided in Appendix B.

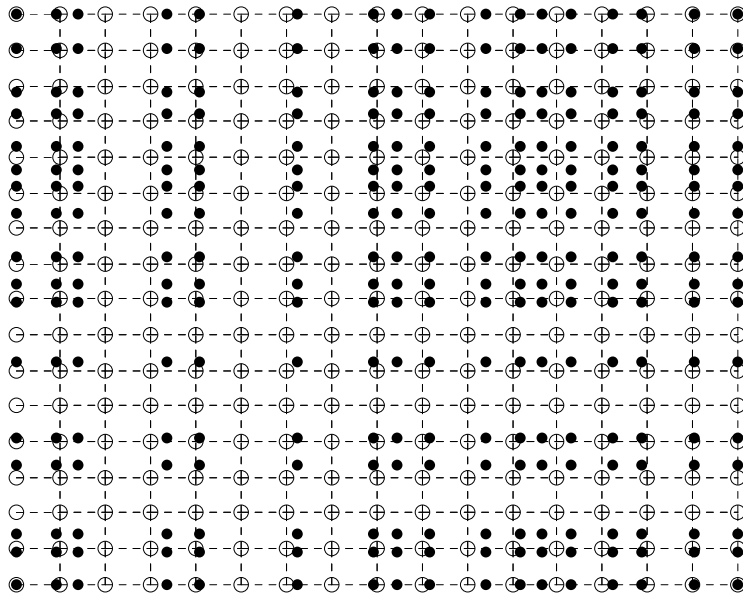
Example 1: Poisson’s equation over a triangular domain

As the first example, the same Poisson equation (40) over a triangular domain (shown in figure 21)

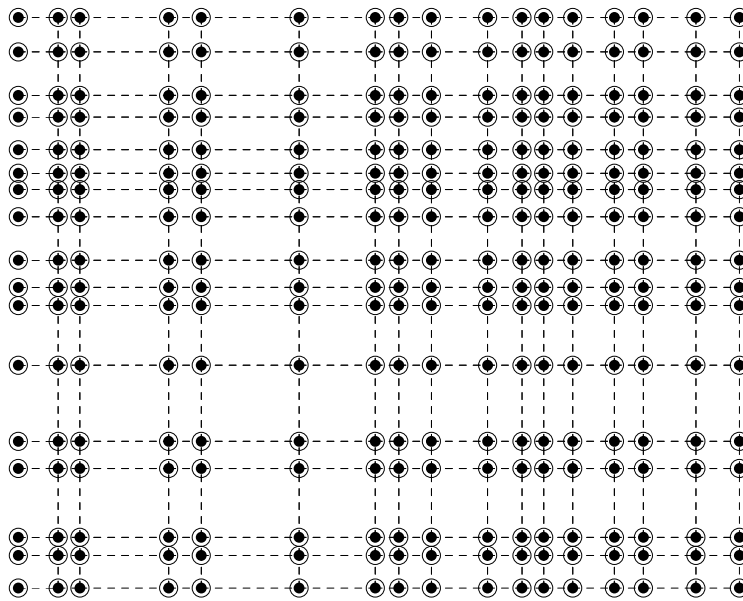
is considered. Since the geometric map for the entire domain is not one-to-one (see figure 3), the domain is decomposed into three ($N^e = 3$) sub-domains as shown in figure 4. Each sub-domain is discretized by $N_p^e = 11 \times 11 = 121$ nodes, which lead to a total of $N_p = 331$ nodes over the entire domain. Errors in the solution are shown in figure 21.

Example 2: A 3D arch subjected to vertical load

As the second example, a 3D arch subjected ver-



(a)



(b)

Figure 19: Typical node and knot distributions in the piecewise NPM in two dimension; (a) uniform knot vector irrespective of the particle distribution; (b) knot points and nodal points are taken the same

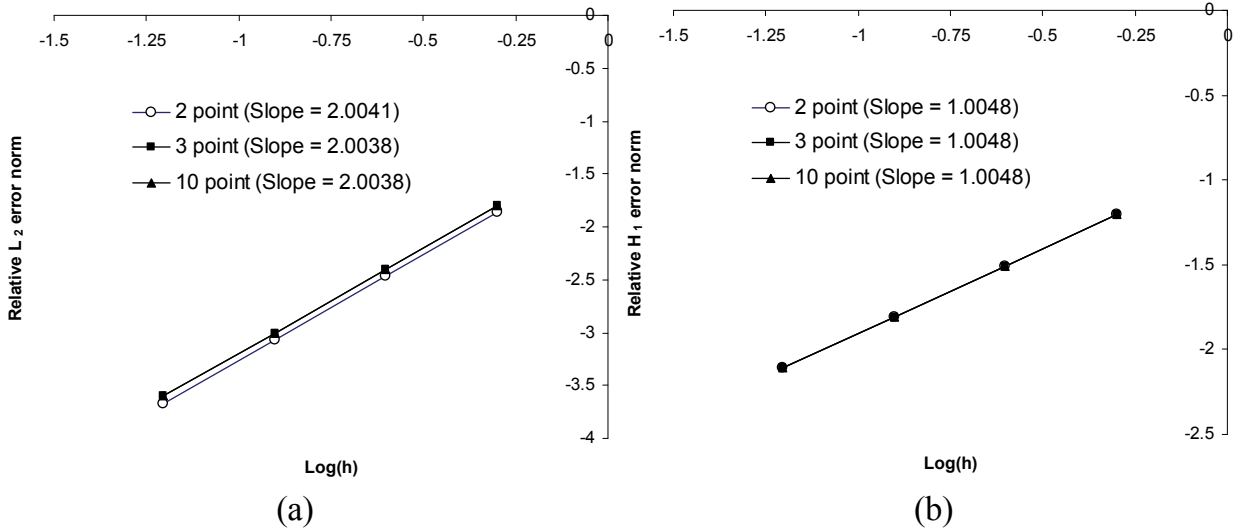


Figure 20: Convergence for different quadrature rules for Poisson’s equation (equation 40); (a) L_2 norm; (b) H_1 norm

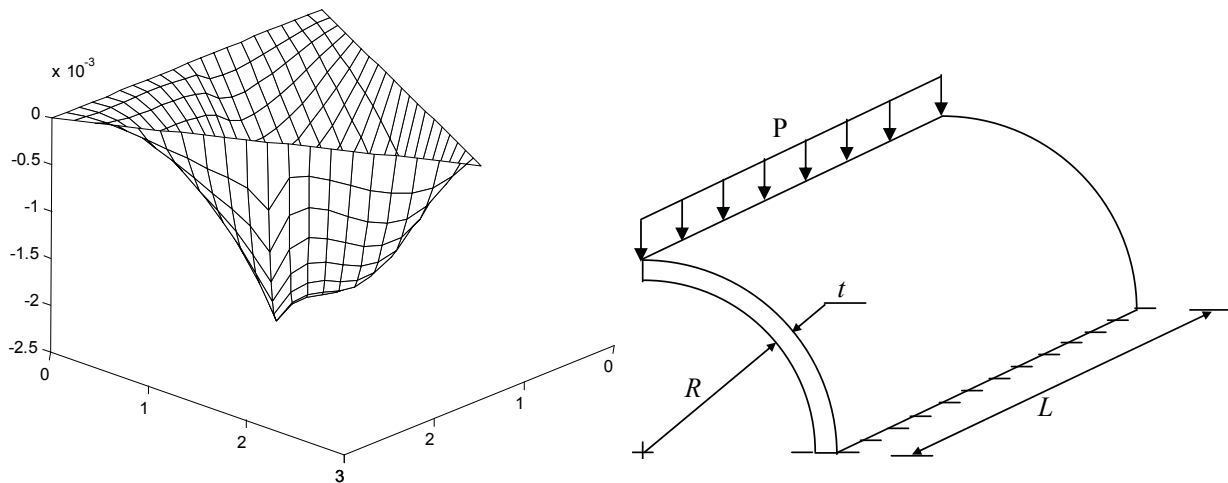


Figure 21: Error in the solution of equation (40); L_2 norm = 9.2×10^{-4} ; H_1 norm = 3.5×10^{-2}

Figure 22: A 3D arch under vertical load

tical load as shown in figure 22 is considered. Dimensions and material constants are given in Table 2. Discretization and corresponding integration cells are shown in figure 23. Note that we use just a single sub-domain for this problem and thus the piecewise NPMM reduces to the usual NPMM. 3D NPMM shape functions are employed. Results are shown in figure 24.

Table 2: Parameters for example 2

Parameter	Value
L	4.0
R	2.0
r	0.2
P	110
Young’s modulus (E)	2×10^5
Poisson ratio (ν)	0.3

Example 3: Hollow cylindrical cantilever beam subjected to vertical load at tip

As the last example, a hollow cylindrical cantilever subjected to a vertical load at the tip is

considered (figure 24). Dimensions and material constants are given in Table 3. The physical do-

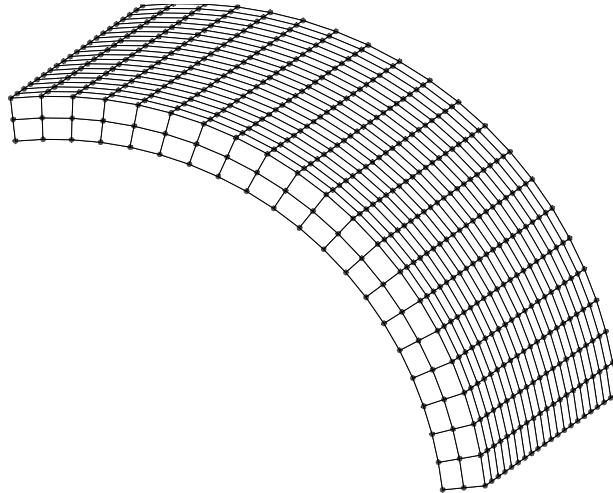


Figure 23: Discretization and the corresponding integration cells

main is decomposed into 4 sub-domains (figure 25) and 3D shape functions are again employed. Discretization and corresponding integration cells are shown in figure 26. Results are shown in figure 27.

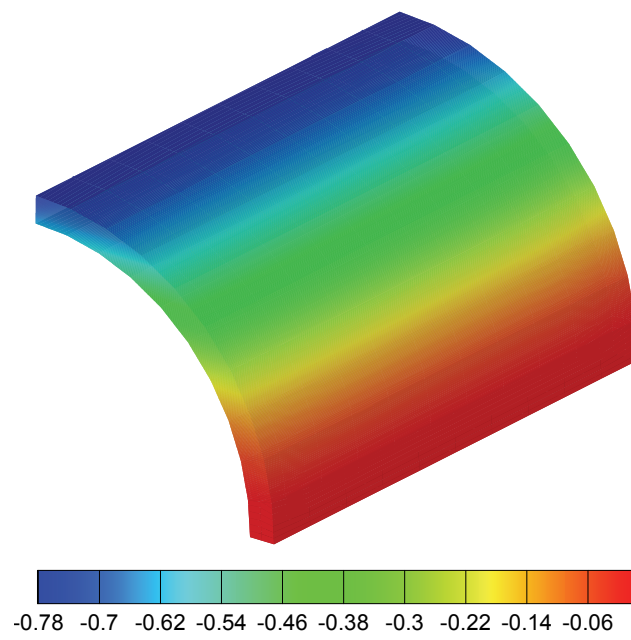
Table 3: Parameters for example 3

Parameter	Value
L	2
R	0.075
r	0.150
P	10
E	2×10^5
ν	0.3

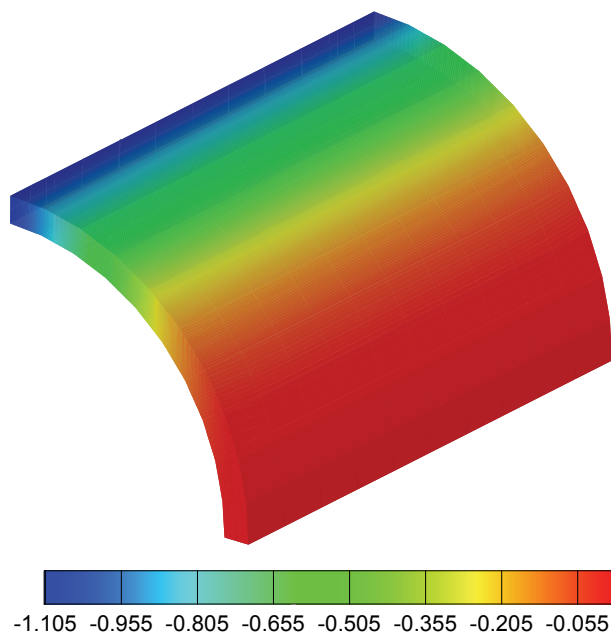
5 The Closure

The piecewise NPMM, considered in this study, is aimed at serving as a seamless bridge between the FEM and mesh-free methods. The method provides a relief from many computational difficulties or limitations present in the FEM (e.g. inaccurate representations of complicated domains, absence of higher order global continuity of shape functions etc.) and most mesh-free methods (choosing an optimal support size of the window function). Yet another noteworthy feature of the piecewise NPMM is that the shape functions as well as the geometric map (over each sub-domain) is constructed

using NURBS, which enables higher order approximations with reduced numerical instability. We also propose novel schemes for endowing the shape functions with the interpolation property and this, in turn, enables enforcement of essential boundary conditions. The interpolating approximation consists of a summation of primitive and NURBS (enrichment) functions such that supports of both the functions coincide. We have attempted using Lagrange polynomials and Deslauriers-Dubuc interpolating wavelets to construct the primitive function. While Lagrange polynomial works well for smaller consistency ($p \leq 2$), it exhibits oscillations in the shape function as p increases. For achieving higher consistency, we use interpolating wavelet basis as the primitive function. Finally, a knot-grid conformal integration scheme for weak implementations of the piecewise NPMM is also proposed. The essence of the scheme is that the functional in the weak form is integrated over a grid formed by the knot vectors. Since B-spline basis functions (a main constituent of NPMM shape functions) are compactly supported between two appropriate knot points (depending on the polynomial order of B-splines), supports of B-spline basis functions are always perfectly aligned with the grid formed by the knot vectors. Consequently the non-conformability arising out of a possible misalignment of support domains and the background mesh is bypassed with very little effort.



(a)



(b)

Figure 24: Contour plots for (a) horizontal displacements u and (b) vertical displacements v

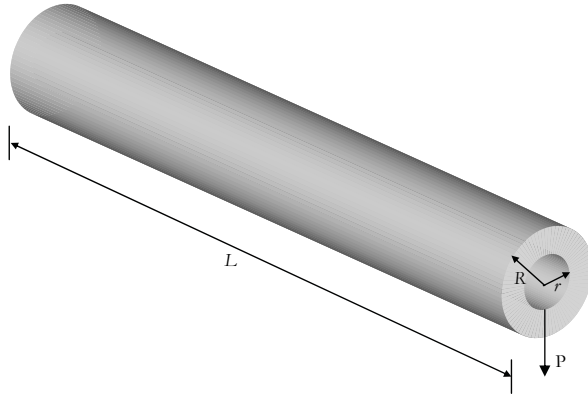


Figure 25: Hollow cylindrical cantilever beam subjected to a vertical load at the tip

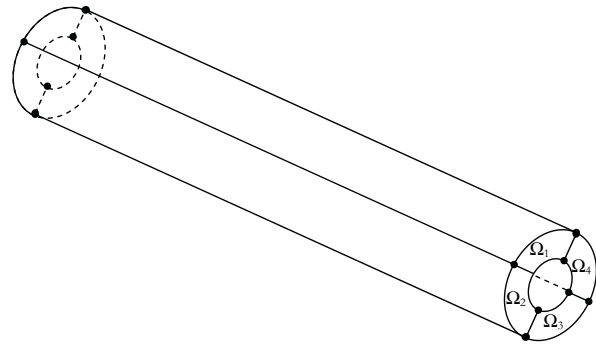


Figure 26: Decomposition of the physical domain (see figure 24) into 4 sub-domains

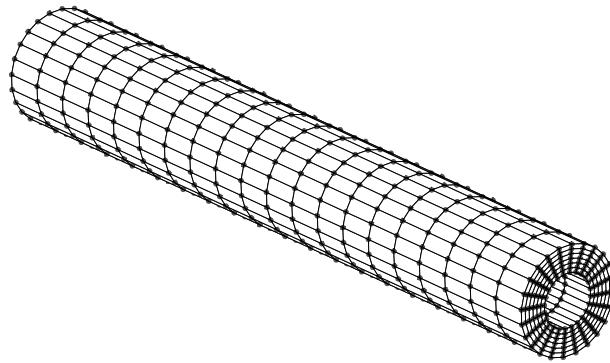


Figure 27: Discretization and corresponding integration cells; $N_p^e = 7 \times 7 \times 21 = 1029$ for $e \in [1, 4]$ and $N_p = 3528$

Acknowledgement: Financial grant from the Vikram Sarabhai Space Centre (VSSC) of the Indian Space Research Organization in conducting this research is gratefully acknowledged.

References

Atluri, S.N.; Han, Z.D.; Rajendran, A.M. (2004): A new implementation of the meshless finite volume method, through the MLPG "Mixed" approach, *CMES: Computer Modeling in Engineering & Sciences* 6(6), 491-513.

Atluri, S.N.; Kim, H.G., Cho, J.Y. (1999): A critical assessment of the truly Meshless local Petrov-Galerkin (MLPG) methods, *Computational Mechanics*, 24, 348-372.

Atluri, S.N.; Liu, H.T.; Han, Z.D. (2006a): Meshless Local Petrov-Galerkin (MLPG) Mixed Finite Difference Method for Solid Mechanics,

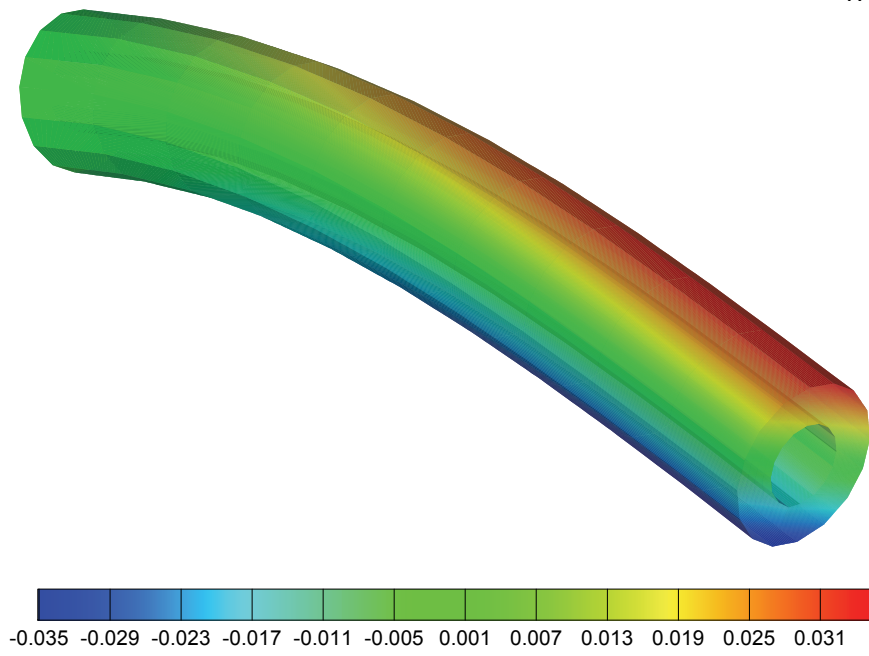
CMES: Computer Modeling in Engineering & Sciences, 15(1), 1-16.

Atluri, S.N.; Liu, H.T.; Han, Z.D. (2006b): Meshless Local Petrov-Galerkin(MLPG) Mixed Collocation Method for Elasticity Problems, *CMES: Computer Modeling in Engineering & Sciences*, 14(3), 141-152.

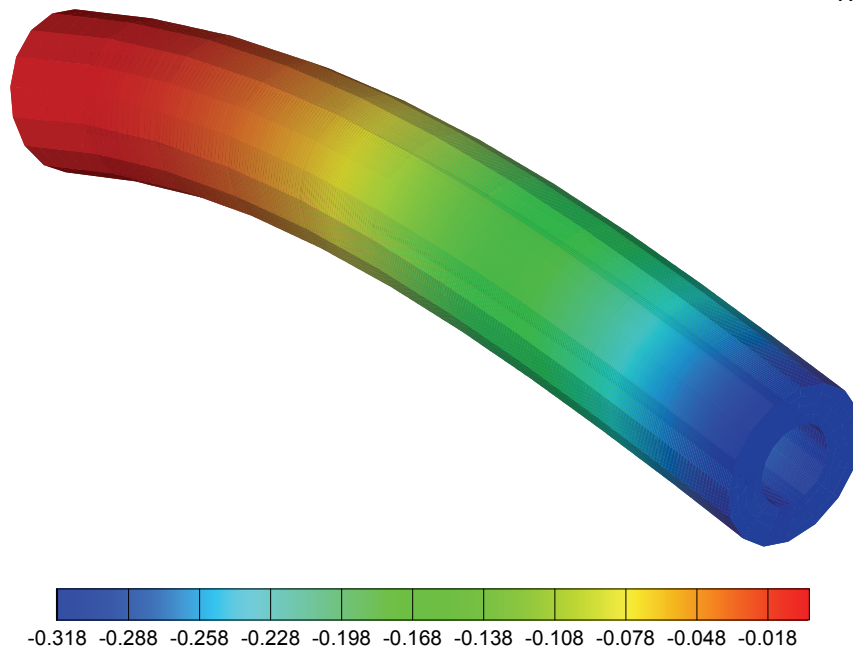
Atluri, S.N.; Shen, S.P. (2002b): The meshless local Petrov-Galerkin (MLPG) method: A simple & less-costly alternative to the finite element and boundary element methods, *CMES: Computer Modeling in Engineering and Sciences*, 3(1), 11-51.

Atluri, S.N.; Zhu, T. (1998): A New Meshless Local Petrov-Galerkin (MLPG) Approach in Computational Mechanics, *Computational Mechanics*, 22, 117-127.

Babuška, I.; Melenk, J.M. (1997): The partition



(a)



(b)

Figure 28: Contour plots for (a) horizontal displacements u and (b) vertical displacements v

of unity method, *Int. J. Numer. Methods Eng.*, 40, 727-758.

Belytschko, T.; Lu, Y.Y.; Gu, L. (1994): Element-free Galerkin methods, *Int. J. Numer. Meth. Eng.*, 37, 229-256.

Chen, J.S.; Han, W.; You, Y.; Meng, X. (2003): Reproducing kernel method with nodal interpolation property, *International Journal for Numerical Methods in Engineering*, 56, 935-960.

Daubechies, I. (1988): Orthogonal Bases of Compactly Supported Wavelets, *Commun. Pure Appl. Math.*, 41, 909-996.

Daubechies, I. (1992): *Ten Lectures on Wavelets*, SIAM, Philadelphia.

Deslaurier, G.; Dubuc, S. (1989): Symmetric Iterative Interpolation Processes, *Constr. Approx.*, 5, 49-68.

Donoho, D.L. (1992): *Interpolating Wavelet Transforms*, Technical Report. Dept. of Statistics, Stanford University, Stanford.

Dolbow J.; Belytschko T. (1999): Numerical integration of the Galerkin weak form in meshfree methods, *Comput. Mech.*, 23, 219-230.

Duarte C.A.; Oden, J.T. (1997): An h-p adaptive method using clouds, *Computer Methods in Applied Mechanics and Engineering*, 139, 237-262.

Fernández-Méndez, S.; Huerta, A. (2004): Imposing essential boundary conditions in mesh-free methods, *Compt. Methods Appl. Mech. Eng.*, 193, 1257-1275.

Fries. T.P.; Matthies, H.G. (2004): Classification and Overview of Meshfree Methods, *Informatikbericht* Nr.: 2003-3.

Gingold, R.A.; Monaghan, J.J. (1977): Smoothed particle hydrodynamics: theory and application to non-spherical stars, *Monthly Notices of the Royal Astronomical Society*, 181, 275-389.

Gu, Y.T.; Liu, G.R. (2001): A boundary point interpolation method for stress analysis of solids, *Computational Mechanics*, 28(1), 47-54.

Han, W.; Meng, X. (2001): Error analysis of the reproducing kernel particle method, *Comput. Methods Appl. Mech. Engrg.*, 190, 6157-6181.

Li, S.F.; Liu, W.K. (2002): Meshfree and particle methods and their applications, *Appl Mech Rev.*, 55(1), 1-34.

Li, S.; Lu, H.; Han, W.; Liu, W.K. (2004): Reproducing Kernel Element Method, Part II Globally Conforming I^m/C^n Hierarchies, *Computer Methods in Applied Mechanics and Engineering*, 193, 953-987.

Liu, G.R.; Gu, Y.T. (2001a): A local point interpolation method for stress analysis of two-dimensional solids, *Strut. Eng. Mech.*, 11(2), 221-236.

Liu, G.R.; Gu, Y.T. (2001b): A local radial point interpolation method (LR-PIM) for free vibration analysis of 2-D solids, *J. Sound Vib.*, 246(1), 29-46.

Liu, G.R.; Gu, Y.T. (2001c): A point interpolation method for two-dimensional solids, *International Journal for Numerical Methods in Engineering*, 50, 937-951.

Liu, W.K.; Han, W.; Lu, H.; Li, S. (2004): Reproducing Kernel Element Method, Part I Theoretical Formulation, *Computer Methods in Applied Mechanics and Engineering*, 193, 933-951.

Liu, W.K.; Jun, S.; Li, S.; Adee, J.; Belytschko, T. (1995b): Reproducing kernel particle methods for structural dynamics, *International Journal for Numerical Methods in Engineering*, 38, 1655-1679.

Liu, W.K.; Jun, S.; Zhang, Y.F. (1995a): Reproducing kernel particle methods, *International Journal for Numerical Methods in Fluids*, 20, 1081-1106.

Liu, W.K., Li, S.; Belytschko, T. (1997): Moving least square reproducing kernel methods (I) methodology and convergence, *Computer Methods in Applied Mechanics and Engineering*, 143, 113-154.

Lu, H.; Li, S.; Simkins, D.C.; Liu, W.K.; Cao, J. (2004): Reproducing Kernel Element Method Part III. Generalized Enrichment and Applications, *Computer Methods in Applied Mechanics and Engineering*, 193, 989-1011.

Lu, Y.Y.; Belytschko, T.; Gu, L. (1994): A new implementation of the element free Galerkin

method, *Computer Methods in Applied Mechanics and Engineering*, 113, 397-414.

Lucy, L.B. (1977): A numerical approach to the testing of the fission hypothesis, *Astrophys. J.*, 82, 1013-1024.

Melenk, J.M.; Babuška, I. (1996): The partition of unity finite element method: Basic theory and applications, *Comput. Methods Appl. Mech. Engrg.*, 139, 289-314.

Monaghan, J.J. (1992): Smoothed particle hydrodynamics, *Annu. Rev. Astron. Astrophys.*, 30, 543-574.

Nayroles, B.; Touzot, G.; Villon, P. (1992): Generalizing the finite element method: diffuse approximation and diffuse elements, *Computational Mechanics*, 10, 307-318.

Piegl, L.; Tiller, W. (1995): *The NURBS Book*, Springer, Berlin.

Shaw, A.; Bendapudi, S.; Roy, D. (2008): A Kriging-based Error Reproducing and Interpolating Kernel Method for Improved Mesh-free Approximations, *International Journal for Numerical Methods in Engineering*, 73, 1434-1467.

Shaw A. (2007): *NURBS-based mesh-free and finite element methods in computational mechanics*, Doctoral thesis, Indian Institute of Science.

Shaw, A.; Roy, D. (2007a): A NURBS-based Error Reproducing Kernel Method with Applications in Solid Mechanics, *Comput. Mech.*, 40(1), 127-148.

Shaw, A.; Roy D. (2007b): A novel form of reproducing kernel interpolation method with applications to nonlinear mechanics, *CMES: Computer Modeling in Engineering and Sciences*, 19(1), 69-98.

Shaw, A.; Roy, D. (2008): NURBS-based Parametric Mesh-free Methods, *Computer methods in applied mechanics and engineering*, 197, 1541-1567.

Simkins, D.C.; Li, S.; Lu, H.; Liu, W.K. (2004): Reproducing Kernel Element Method Part IV. Globally Conforming C^n ($n \geq 1$) Triangular Hierarchy, *Computer Methods in Applied Mechanics and Engineering*, 193, 1013-1034.

Zhu, T.; Zhang, J.; Atluri, S.N. (1998): A

meshless local boundary integral equation (LBIE) method for solving nonlinear problems, *Computational Mechanics*, 22, 174.

Appendix A: Interpolating Wavelets

In this appendix, we briefly recall the properties of wavelets (especially interpolating wavelets). Wavelets are characterized by the translation and dilation of a single function $\psi(x)$. Wavelets can be real or complex functions. The wavelet function $\psi(x)$ is generated by another function called scaling function $\phi(x)$. In case of Daubechies family, neither the scaling function nor the wavelet has a closed-form expression. They are both finitely (compactly) supported; i.e., they are identically zero outside of a finite interval. Compactly supported wavelets are differentiable and form a set of orthonormal basis functions with localization and scaling properties.

The Daubechies scaling function $\phi(x)$ of rank 2 and genus N is defined by the two-scale relation (Daubechies, 1988, 1992):

$$\phi(x) = \sum_{k=0}^{2N-1} p_k \phi(2x-k) \quad j, k \in Z \quad \dots \quad (\text{A-1})$$

Here p_k 's are the filter coefficients. The support of $\phi(x)$ and is $\text{supp}[0, 2N-1]$. A similar expression can be obtained for the wavelet function as well. The interpolating wavelet is obtained by taking the convolution of the scaling function with itself. The Deslauriers-Dubuc interpolating function (Deslauriers and Dubuc 1989), which is the autocorrelation function of the Daubechies scaling function, can be obtained as:

$$\theta(x) = \int_{-\infty}^{+\infty} \phi(y)\phi(y-x)dx \quad \dots \quad (\text{A-2})$$

The function $\theta(x)$ has following properties.

- Compact support between $[-2N+1, 2N-1]$
- Satisfies the two scale relation (1) i.e. $\theta(x) = \sum_{k=-2N+1}^{2N-1} h_k \theta(2x-k)$
- Has vanishing moments of all orders up to $(2N-1)$, which implies that linear combination of $\theta(x)$ can represent polynomials with degree up to $2N-1$

- The approximating bases through dilations and translations of $\theta(x)$ form a set of interpolating bases, i.e. $\theta(x_k) = \delta_{k,0}$

h_k 's are the filter coefficients obtained through the discrete convolution of Daubechies filter coefficients as:

$$h_k = \sum_{m=0}^{2N-1} p_m p_{m-k} \text{ for } k \geq 0 \text{ and } h_{-k} = h_k \dots \quad (\text{A-3})$$

The derivative of the scaling function may be obtained as:

$$\theta^d(x) = (-1)^d \int_{-\infty}^{+\infty} \varphi(y) \varphi^d(y-x) dx \dots (\text{A-4})$$

Any square integrable function $f(x)$ can be approximated in the wavelet basis as:

$$f(x) = \sum_{j=-\infty}^{+\infty} \sum_{k=-\infty}^{+\infty} b(j,k) 2^{j/2} \theta(2^j x - k) \dots \quad (\text{A-5})$$

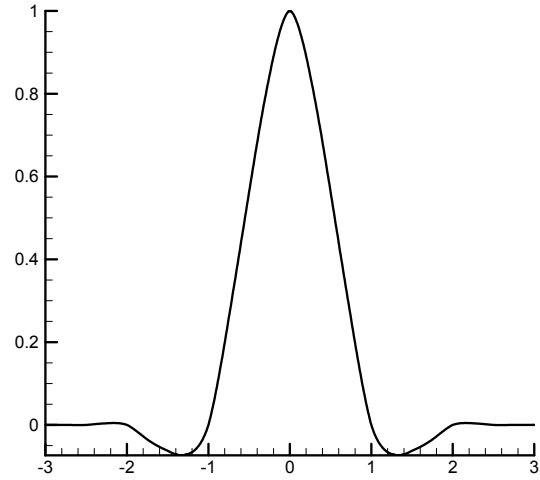
$b(j,k)$ is the discrete wavelet transform (DWT) at scale j and the above expression represents the inverse discrete wavelet transform (IDWT). The formal definition of DWT is given by:

$$\begin{aligned} b(j,k) &= 2^{j/2} \int_{-\infty}^{+\infty} f(x) \theta(2^j x - k) dx \\ &= \int_{-\infty}^{+\infty} f(x) \theta_{j,k} dx \dots \end{aligned} \quad (\text{A-6})$$

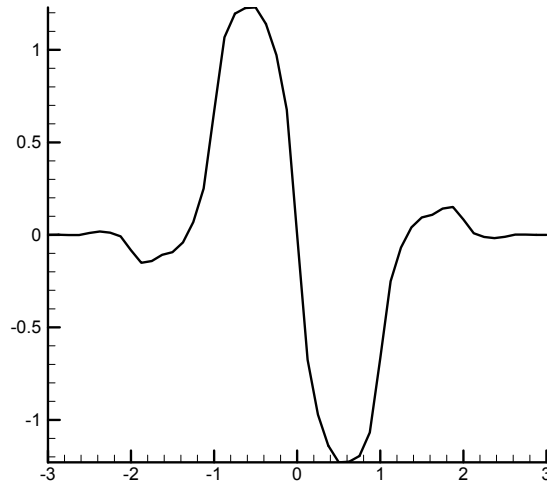
Basically, the function $f(x)$ is approximated by translates of the wavelet bases through an infinite summation over all possible scales.

Appendix B: Geometric Data for NURBS Model Used in Section 5

See Tables B-1, B-2 and B-3.



(a)



(b)

Figure A-1: Deslauriers-Dubuc ($N = 2$) (a) interpolating wavelet and (b) its first derivative

Table B-1: Geometric data for example 1

Patch	Control Points	Knot vector and B-spline
Ω_c^1	$P_1 = (3/2, 1) \quad P_3 = (3/2, 3)$ $P_2 = (9/4, 3/2) \quad P_4 = (3/4, 3/2)$	Linear B-spline over $\Xi^{1g} = \{0, 0, 1, 1\}$ Linear B-spline over $\wp^{1g} = \{0, 0, 1, 1\}$ $\aleph^{1g} = \Xi^{1g} \times \wp^{1g}$ $w_1 = w_2 = w_3 = w_4 = 1$
Ω_c^2	$P_1 = (0, 0) \quad P_3 = (3/2, 1)$ $P_2 = (3/2, 0) \quad P_4 = (3/4, 3/2)$	Linear B-spline over $\Xi^{2g} = \{0, 0, 1, 1\}$ Linear B-spline over $\wp^{2g} = \{0, 0, 1, 1\}$ $\aleph^{2g} = \Xi^{2g} \times \wp^{2g}$ $w_1 = w_2 = w_3 = w_4 = 1$
Ω_c^3	$P_1 = (3/2, 0) \quad P_3 = (9/4, 3/2)$ $P_2 = (3, 0) \quad P_4 = (3/2, 1)$	Linear B-spline over $\Xi^{3g} = \{0, 0, 1, 1\}$ Linear B-spline over $\wp^{3g} = \{0, 0, 1, 1\}$ $\aleph^{3g} = \Xi^{3g} \times \wp^{3g}$ $w_1 = w_2 = w_3 = w_4 = 1$

Table B-2: Geometric data for example 3

Sub-domain	Control Points	Knot vector and B-spline
Ω_c^1	$P_1 = (0, 1.8, 0) \quad P_7 = (0, 1.8, 4)$ $P_2 = (1, 1.8, 0) \quad P_8 = (1.8, 1.8, 4)$ $P_3 = (1.8, 0, 0) \quad P_9 = (1.8, 0, 4)$ $P_4 = (0, 2, 0) \quad P_{10} = (0, 2, 4)$ $P_5 = (2, 2, 0) \quad P_{11} = (2, 2, 4)$ $P_6 = (2, 0, 0) \quad P_{12} = (2, 0, 4)$	Quadratic B-spline over $\Xi^3 = \{0, 0, 0, 1, 1, 1\}$ Linear B-spline over $\wp^3 = \{0, 0, 1, 1\}$ Linear B-spline over $\mathcal{P}^3 = \{0, 0, 1, 1\}$ $\aleph^3 = \Xi^3 \times \wp^3 \times \mathcal{P}^3$ $w_1 = w_3 = w_4 = w_6 = 1$ $w_7 = w_9 = w_{10} = w_{12} = 1$ $w_2 = w_5 = w_8 = w_{11} = 1/\sqrt{2}$

Table B-3: Geometric data for example 3

Sub-domain	Control Points	Knot vector and B-spline
Ω_c^1	$P_1 = (0, -0.075, 0)$ $P_7 = (0, -0.075, 2)$ $P_2 = (-0.075, -0.075, 0)$ $P_8 = (-0.075, -0.075, 2)$ $P_3 = (-0.075, 0, 0)$ $P_9 = (-0.075, 0, 2)$ $P_4 = (0, -0.150, 0)$ $P_{10} = (0, -0.150, 2)$ $P_5 = (-0.150, -0.150, 0)$ $P_{11} = (-0.150, -0.150, 2)$ $P_6 = (-0.150, 0, 0)$ $P_{12} = (-0.150, 0, 2)$	Quadratic B-spline over $\Xi^1 = \{0, 0, 0, 1, 1, 1\}$ Linear B-spline over $\wp^1 = \{0, 0, 1, 1\}$ Linear B-spline over $\mathcal{P}^1 = \{0, 0, 1, 1\}$ $\mathfrak{K}^1 = \Xi^1 \times \wp^1 \times \mathcal{P}^1$ $w_1 = w_3 = w_4 = w_6 = 1$ $w_7 = w_9 = w_{10} = w_{12} = 1$ $w_2 = w_5 = w_8 = w_{11} = 1/\sqrt{2}$
Ω_c^2	$P_1 = (-0.075, 0, 0)$ $P_7 = (-0.075, 0, 2)$ $P_2 = (-0.075, 0.075, 0)$ $P_8 = (-0.075, 0.075, 2)$ $P_3 = (0, 0.075, 0)$ $P_9 = (0, 0.075, 2)$ $P_4 = (-0.150, 0, 0)$ $P_{10} = (-0.150, 0, 2)$	Quadratic B-spline over $\Xi^2 = \{0, 0, 0, 1, 1, 1\}$ Linear B-spline over $\wp^2 = \{0, 0, 1, 1\}$ Linear B-spline over $\mathcal{P}^2 = \{0, 0, 1, 1\}$

